Six-Component Load Cell Design for Use in Force Measurement Platforms

THESIS

Presented in Partial Fulfillment of the Requirements for the Degree Master of Science in the Graduate School of The Ohio State University

By

Benjamin Hoffman

Graduate Program in Mechanical Engineering

The Ohio State University

2013

Master's Examination Committee:

Necip Berme, Advisor

Manoj Srinivasan

Abstract

Force measurement platforms play an important role in the field of biomechanics by allowing for accurate measurement of the ground reaction forces during studies. Several varieties of forces measurement platforms are available on the market, although strain gage based force platform are most prevalent. This thesis details the design of a 6-component load cell consisting of a machined aluminum cylinder with attached strain gages for use in force platforms. The load cell design is intended to improve accuracy, increase the natural frequency, and improve the calibration process for strain gage based force measurement platforms. The performance of different load cell geometries were tested using finite element analysis to determine strain levels. Once optimal load cell geometries were determined, two sets of load cells were manufactured and implemented in a full force platform assembly. While one of the prototype load cell designs proved to be ineffective in final installation, the other design slightly improved the natural frequency, maintained the accuracy, and allowed for a simplified calibration process.

Acknowledgements

I would like to give a special thanks to all of the engineers and technicians of Bertec Corporation. Without their support during the preliminary design and prototype fabrication, this research would not have been possible.

Vita

2011.....B.S. Mechanical Engineering, Ohio State University.

2013 Expected Graduation .....M.S. Mechanical Engineering, Ohio State University.

Fields of Study

Major Field: Mechanical Engineering

Table of Contents

List of Tables

List of Figures

Chapter 1: Introduction and Background

1.1: Inverse Dynamics Method

The field of biomechanics relies heavily on the measurement of loads acting on the human body and joints. Due to the difficulty in obtaining direct measurement of loads on joints (Brand, Crowninshield, Johnston, & Andrews, 1978), the inverse dynamics method is commonly used to calculate joint loads based on kinetic and known load data (Bisseling & Hof, 2004). Inverse dynamics allows for the calculation of loads and moments on the human body based on the known kinetic, mass and inertia properties of the body parts. Two approaches to the inverse dynamic problem can be used to determine joint moments and loads. The first approach, the top-down approach, uses the kinematic data of the upper body to calculate the lower body joint loading (Riemer, Hsiao-Wecksler, & Zhang, 2008). The second approach, the bottom-up approach, calculates the joint loading based on lower body kinematics and ground reaction forces (GRF) acting on the foot. Since it is generally easier to measure GRF's than to accurately estimate upper body kinematics (Desjardins, Plamondon, & Gagnon, 1998), the bottom-up approach is generally favored to obtain more accurate inverse dynamics solutions. However, the accuracy bottom-up inverse dynamics solutions are limited by accuracy of the device being used to measure the ground reaction forces.

1.2: Force Plates

Several alternatives are in use for the measurement of GRF in biomechanical studies. Measurement of GRF's can be achieved by using a platform instrumented with force transducers. When the subject walks, runs, or jumps on the force plate during a study, the force transducer can act as a high precision scale to measure the vertical and shear GRF, as well as the position of the center of pressure (CoP) of the loads. Each individual force platform uses multiple load cells in conjunction to calculate the CoP, moments, and GRF's acting at any point in the platform, typically with one load cell in each corner of a rectangular plate. Two common types of force transducers used in force measurement platforms are piezoelectric based load cells and strain gauge based load cells. Piezoelectric load cells utilize piezoelectric material in disk form to generate an electrical charge in response to changes in stress due to compressive loads. In general, piezoelectric force platforms are best suited for dynamic loading situations due to the loading changes required to generate the electrical charge in the sensor. In static or near static loading conditions, the piezoelectric crystals tends to lose charge and measurement accuracy (Lord, 1981). Strain gauge based force platforms are far more prevalent in the biomechanics field due to their adaptability to both static and dynamic loading conditions. These type of force transducers are composed of elements that deform under and applied load, resulting in a change in resistance of the attached strain gages. By applying a current to the strain gages, the resulting to voltage changes may be used to calculate the applied load. The accuracy, sensitivity, and resonance of strain gauge force platforms is determined by the geometry and structure of the gauged material acting as

the load cell, as well as the arrangement and orientation of the strain gages on the deformed surface. A 1952 University of California study with the purpose of obtaining information to assist in the development of artificial limbs was one of the first research efforts to use a utilize a strain gage based force platform that could measure vertical force, lateral shear force, and fore-aft shear (Cunningham & Brown, 1952). The force platform design consisted of two parallel plates connected by four hollow gaged cylinders called "pylons". A photograph of this force platform design by Brown and Cunningham can be seen in Figure 1.

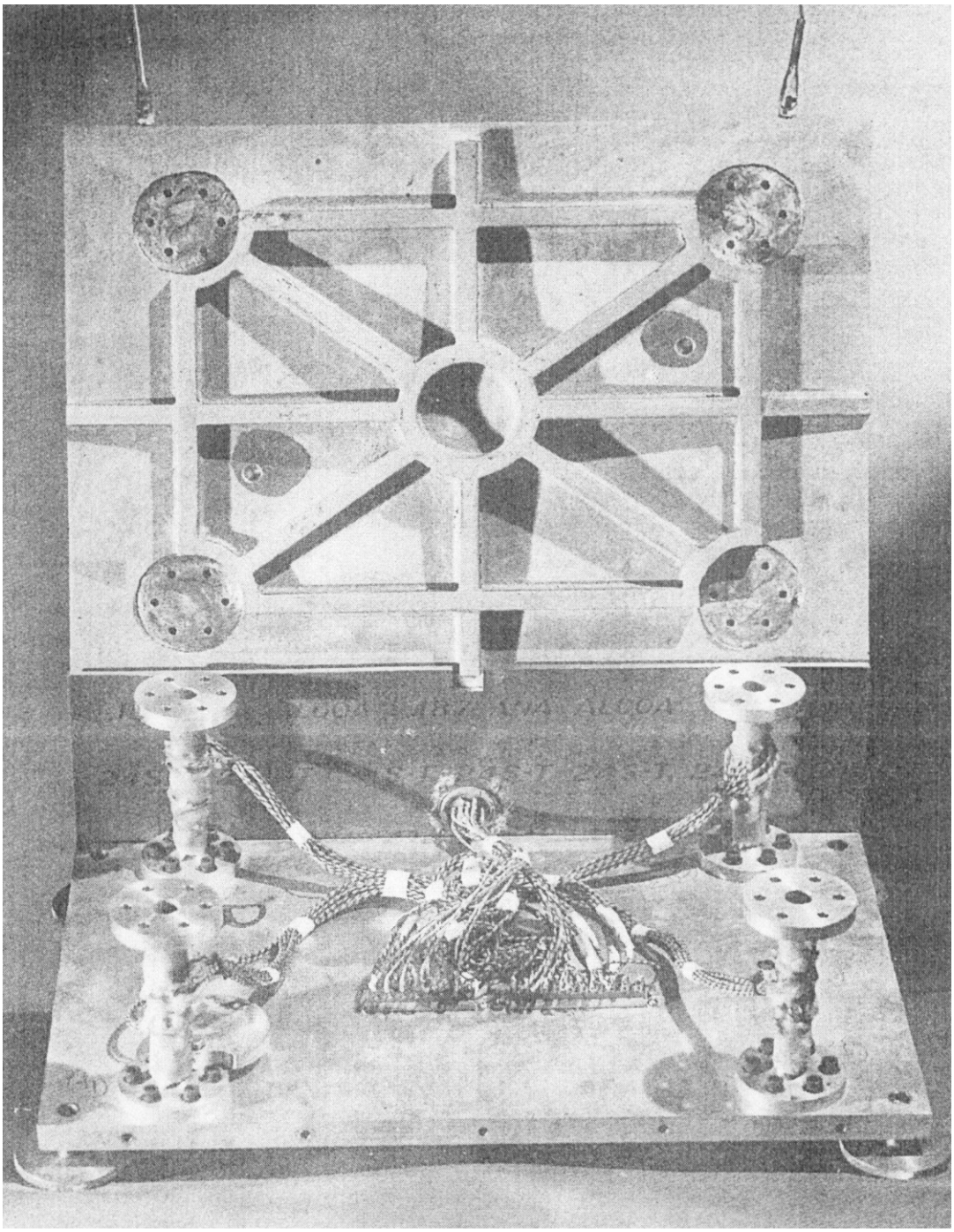

Figure 1: Cunningham and Brown's Gaged Pylon Based Force Plate Design (Brown 1952).

Over the years, design improvements to force plates have focused getting plate design closer to an "ideal" force plate in several key characteristics. Heglund (1981) described an ideal force plate as one that can determine the three force components, have low crosstalk between measured force components, have adequate sensitivity for the subject, have a linear response which is independent of the point of application, have a high natural frequency, and be safe and inexpensive. Indeed, force platform stiffness has been noted to be a potential cause of errors on force plate measurement and calibration (Chockalingam, Nachiappan, Giakas, & Iossifidou, 2002). Advanced Mechanical Technology Inc. (AMTI) made a force measuring biomechanics platform commercially available 1980's which utilized the strain gage based load cell design (U.S. Patent No. 4,493,220, 1985). The platform included four tubular shaped load cells located between two parallel plates in a configuration as shown in Figure 2. The load cell design included a two piece hollow tubular column that is bolted centrally to both the top platform and base plate, as shown in Figure 3.

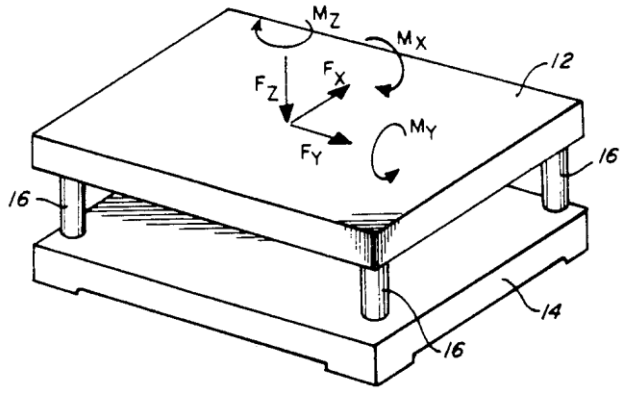

Figure 2: Patent Drawing of AMTI Force Measurement Platform Design (U.S. Patent No. 4,493,220, 1985).

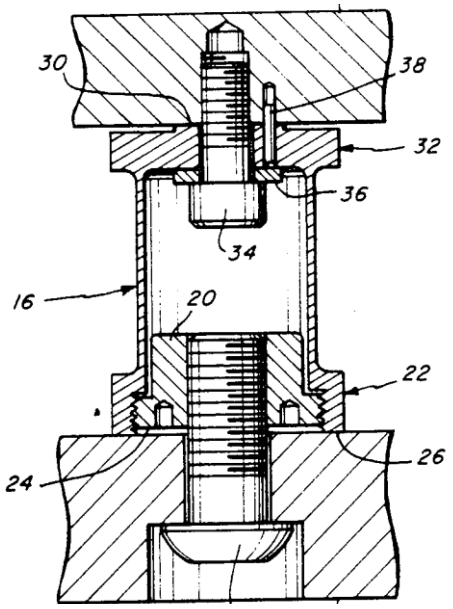

Figure 3: Patent Drawing of AMTI Force Platform Load Cell (U.S. Patent No. 4,493,220, 1985).

Each individual tubular load cell were instrumented with strain gages to measure the vertical (F_z), horizontal shears (F_x and F_y) as well the moments about the three axes (M_x, M_y, M_z). The flat layout of the gages about the tubular load cell, shown in Figure 4, allows the shear strains to be measured loads to be measured by gages 1, 2, 5, 6, 9, and 10. The vertical strains are measured by 3, 4 , 7, and 8. The moments M_x and M_y are measured by the strains in gages 11, 12 , 13, and 14. This layout allowed some gages to be highly sensitive to individual components of vertical loads, shear loads, or moments, thus reducing the potential for "crosstalk", or erroneous load measurements from the gages under combined stresses.

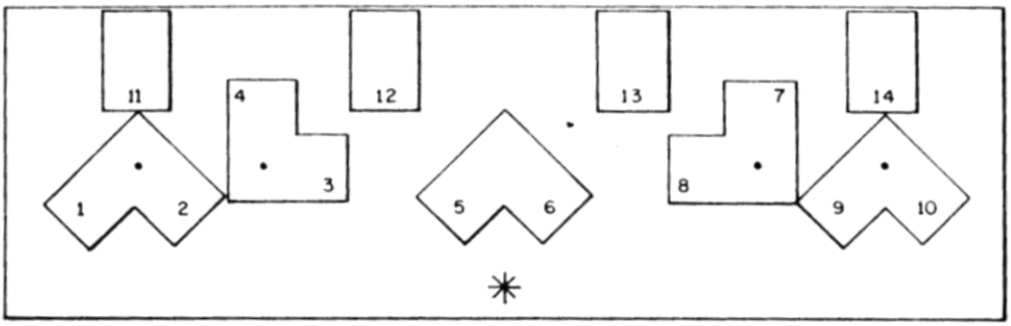

Figure 4: Layout of Strain Gages on a AMTI Force Platform Load Cell.

The concepts of the gaged tubular load cell was further refined by Bertec Corporation designs in the 2000's. In order to completely eliminate the erroneous crosstalk signals when calculating moments between load cells, Bertec force platforms included four load cells that each independently measure the vertical, two shear, and one moment about each axis (U.S. Patent No. 6,295,878 B1, 2001). This concept of independent load cells greatly reduces the amount of error induced when calculating the loads, moments, and CoP acting on the top plate of the force platform, especially in platforms involving larger spans (U.S. Patent No. 6,354,155 B1, 2002). Additionally, having interdependent load cells within each platform requires that it be calibrated as a unit once assembled, rather than having each load cell calibrated before assembly.

1.3: Force Measurement Treadmills

Force biomechanics studies requiring collection of walking or running gait data, traditional force measurement platforms often do not provide the surface area necessary to collect significant amounts of data Additionally, it can be difficult for subjects and patients with limited mobility or motor skills to accurately place their feet on the force platforms. To measure a more than a few step of subject gait data, alternatives to the basic force plate design were investigated. Some studies (Miyazaki & Iwakura, 1978) eliminated the force plate and instead used a load cell fixed in a subjects shoe. Unfortunately, alternative load measurement devices such as shoe mounted load cells lack the accuracy and repeatability of traditional force plates. Consequently, for biomechanics applications that require the collection of large amounts of gait data, several force platform designs have been integrated into treadmills to allow for continuous collection of gait data from subjects. Early force measurement treadmills (Kram, Griffin, Donelan, & Chang, 1998) Struggled with accuracy in the measurement of some of the shear loads and moments. Some more recent treadmills (Dieriek, Penta, Renaut, & Detrembleur, 2004) improved on shear measurement accuracy, but still had undesirable natural frequencies below 40Hz and required further reduction in center of pressure error and cross talk. Indeed, load measurement errors of more than 20 N are possible (Belli, Bui, Berger, Geyssant, Lacour, 2001), and cross talk, non-linearity, frame stiffness are problems that continue to persists for treadmill force plate designs. The introduction of the treadmill to the force platform design brings several challenges. One common design for instrumented treadmills is the split belt configuration shown in Figure

5. This setup includes two separate instrumented treadmills, allowing the impact loads of the right and left feet may be measured independently.

Figure 5: Fully Assembled Dual Belted Bertec Force Measurement Treadmill.

1.4: Pylon Design

Initial Bertec treadmill designs did not utilize the six component load cells, and instead used a half-bridge load cell design that required that the treadmill force platform be calibrated after the treadmill was completely assembled and attached to the base mounting plate. The load cell design featured a tubular aluminum element with an external top and bottom flange mounting to the treadmill base and base mounting plate respectively. The current Bertec treadmill load cell design is shown in Figure 6.

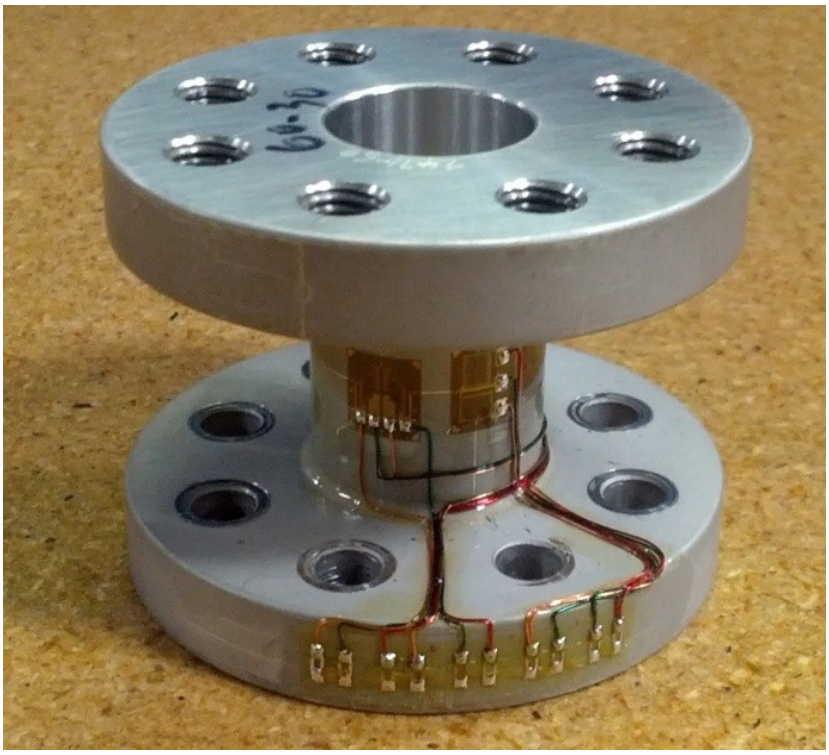

Figure 6: Standard Bertec Pylon Load Cell

Although numerous advances to force measurement platform and instrumented treadmill design have occurred over the past decade, several design, calibration, and

production issues still require significant improvement. Overall, the treadmill design is large and heavy, due to the requirement that the force platform have minimal deflection to allow for accurate force measurements by the load cells. Additionally, the natural frequency of the load cells must be sufficiently high to avoid the addition of unwanted low frequency vibrations to biomechanics signals. Because most Biomechanics signals are of a low order of frequency of 1-10 Hz a natural frequency of 45-60 hertz is sufficient for data collection without filtering.

The purpose of this project is to investigate possible methods for improving the design of Bertec force measurement platforms, particularly those integrated into treadmill systems. There are several areas of focus for potential improvement. The mechanical design of the load cell should be modified to allow the load cell to be mounted and dismounted without altering the calibration of the gages. It is also desirable to improve the natural frequency of the load cell, or at a minimum maintain the current natural frequency. In addition to the mechanical design requirements, the load cell calibration process must also be improved to allow the load cells to be calibrated independently with six components, and then transferred to the force platform surface after calibration is complete. Because load cell calibration is currently a manual process that is both time consuming and has potential for inaccuracies do to human error , the calibration process needs to be refined to allow for calibration of individual load cells, potentially in an automated calibration device.

Chapter 2: Methods

The purpose of this study is to improve the pylon load cell design so that the load cell boundary conditions are isolated from the mounting conditions on both the bottom surface of the treadmill as well as floor mounting surface. This improvement will allow the pylons to be calibrated individually as 6-component load cells, then transferred at a later time to the completed treadmill assembly. Additionally, it is desirable to maintain the current pylon height and capability of fastening a completed force platform to the floor using a access through the hollow center of the pylon. Also, the natural frequency of the pylon should be at a minimum maintained at the current level of 45-60 Hz, although increasing the natural frequency can be considered a secondary benefit of any pylon design changes.

Initial brainstorming of the pylon focused on several pylon design features to determine their effect on pylon performance in the final force platform assembly. Design features to be investigated included the pylon diameter, shaft height, shaft geometry, mounting flange thickness, and mounting flange diameter. Pylon performance was determined by using finite element analysis software, Solid Edge Nastran, to determine strain levels at the gaged section of the pylon. The two types of gages used on the pylon surface, Vishay J2A-13-S036R-350/SP62 for shear loads and J2A-13-S114L-350/SP62 for axial loads, have a maximum rated strain to failure of 2000με. This maximum strain

also corresponds to the maximum designed load rating of the pylons of 2000 lbs. In this study, several pylon geometries were tested under various loading conditions to simulate imperfect mounting conditions on the assembled force platform and mounting plate. The goal was to determine which pylon geometries would limit the strain at the gaged potion of the pylon to a minimum, and to ensure that the boundary conditions of the pylon do not affect previous calibration data.

Three pylon loading conditions were considered for simulation. The first pylon loading condition simulates the mounting surfaces on either side of the pylon being out of parallel by 5/1000" across a distance of 8", which is a relatively common mounting condition for pylons due to the allowable tolerance in the manufacturing process of both the mounting plates and pylon surfaces. The second loading condition involves the simulation of clamping load of a single #10-32 socket head cap screw on the mounting flange of the pylon. Although the clamping load of the screws can vary depending on lubrication and thread material contact, the simulated clamping load used in this study was set at 2100 lbs resulting from an 85 in-lb tightening torque. The third and final loading condition examined was a deformation of the pylon mounting flange, caused by one end of the pylon being mounted on a surface with local irregularities or non-flatness. Although these three loading conditions do not encompass all possible loading conditions, they do represent common conditions that the pylon design must be robust enough to adapt to without losing calibration or accuracy.

2.1: FEM Loading Conditions

In order to set a baseline to compare potential design alterations, the three finite element loading conditions were simulated for the current Bertec pylon design. Figure 7 shows the results of the non-parallel mounting surfaces for the pylon. Based on FEM simulation of this loading condition, there is an induced strain in the shaft of the pylon that approaches 600με. Although still within the allowable limits of the strain gauges, this mounting condition adds a considerable preload to the pylon during mounting.

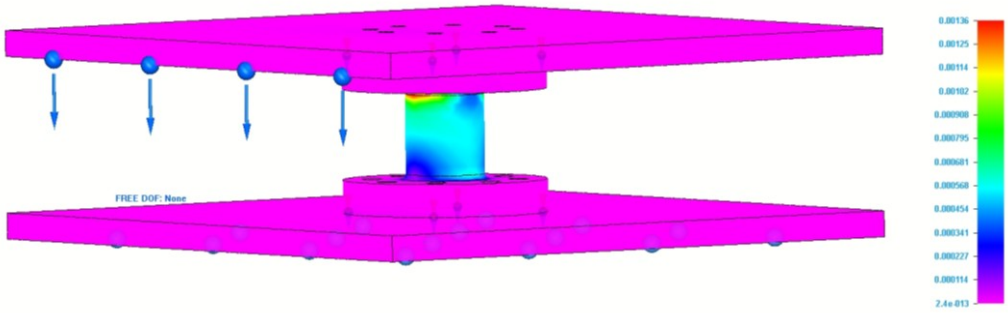

Figure 7: Non-Parallel Loading Condition for Standard Pylon

The second loading condition tested was clamping load due to the screw preload on the pylon mounting flange. For the FEM simulation, a single screw was placed in the model with a 2100 lb preload applied. In actual application, 8 screws would be used to mount the pylon to each surface. In order to simplify the simulation, it was assumed that the 85 in-lb torque applied to the screw would be negligible relative to the 2100 lb clamping load. The results of the FEM simulation are shown in Figure 8. The screw preload induces a strain near the central gaged area of the pylon of up to 30με, a

strain level high enough to cause any calibration to be invalidated if the pylon is dismounted and repositioned.

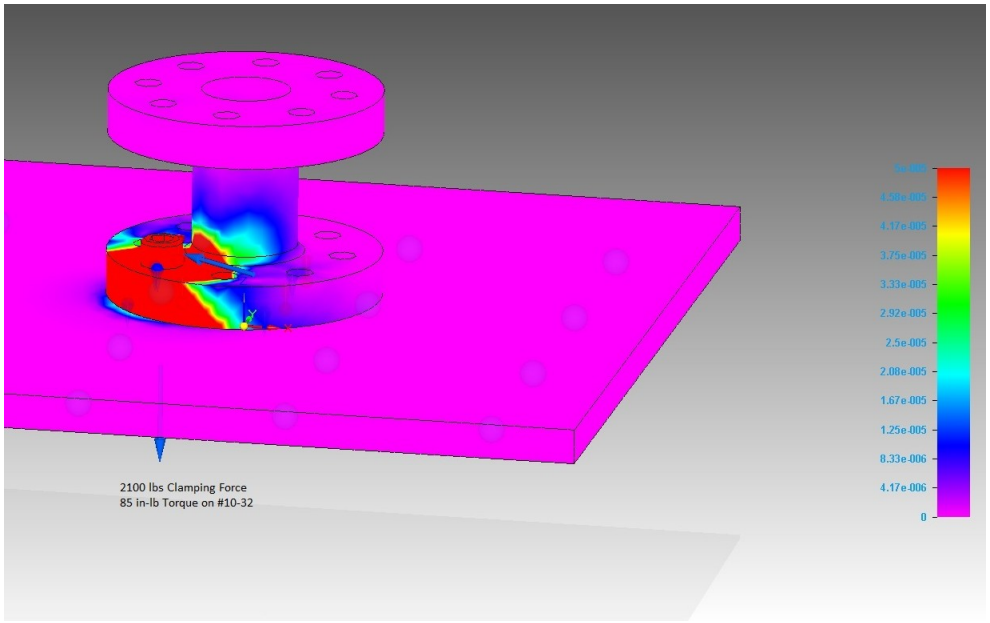

Figure 8: Screw Loading Condition for Standard Pylon.

The third loading condition simulation, shown in Figure 9 shows the results of a local deformation of the pylon flange. Deforming the flange by 0.005” at the screw through hole location, the induced strain at the gaged section of the pylon shaft approaches 50με, a result similar in magnitude to the screw clamping induced strain. Additionally, the when the flange is deformed in this loading condition, a secondary effect of the load is the loss of circularity of the pylon shaft. This folding deformation, scaled to 5% of the model size, is shown in Figure 10, can cause the calibration equations to be inaccurate due simply to the geometry change of gaged mounting area.

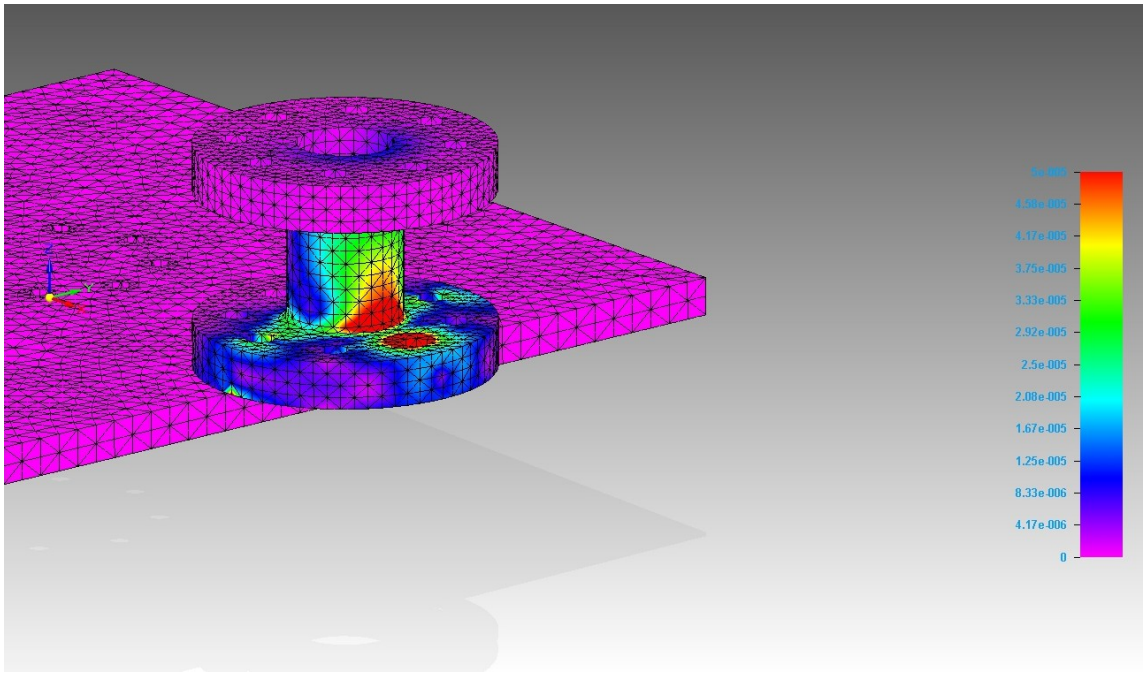

Figure 9: Standard Pylon with Local Flange Deformation.

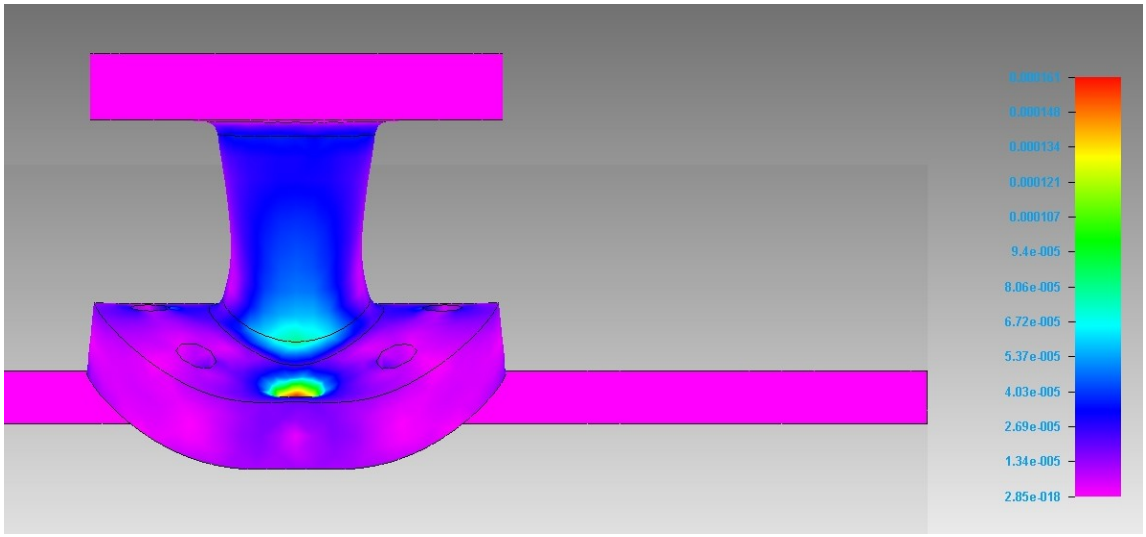

Figure 10: Standard Pylon with Local Flange Deformation, Scaled to 5% of Pylon Size.

2.2: Designs Investigated

Several potential pylon design features were investigated to determine which changes could best isolate the pylon boundary conditions from the strain gage area while maintaining or improving the current pylon's natural frequency. The first pylon design feature to be simulated was the shaft length. A pylon with identical dimensions to original pylon design was altered to have a shaft length of 2.24", which is 1.37" longer than the original design. This elongated pylon was then evaluated using the same FEM loading conditions as the original pylon. The results of the FEM simulation for the non-parallel surface loading condition is shown in Figure 11, the screw preload condition is shown in Figure 12, and the localized flange deformation is shown in Figure 13. As expected, the elongated shaft eliminates the high levels of strain due to the screw preload by moving the gaged area farther from the clamped area on the mounting flange. Additionally, the maximum strain levels observed in the gaged area due to the non-parallel surface loading condition were also reduced for the pylon with elongated shaft, from around 600με to 300με. For the localized pylon flange deformation, strain levels in the gaged area decreased from 45με to 20με for the pylon with elongated shaft.

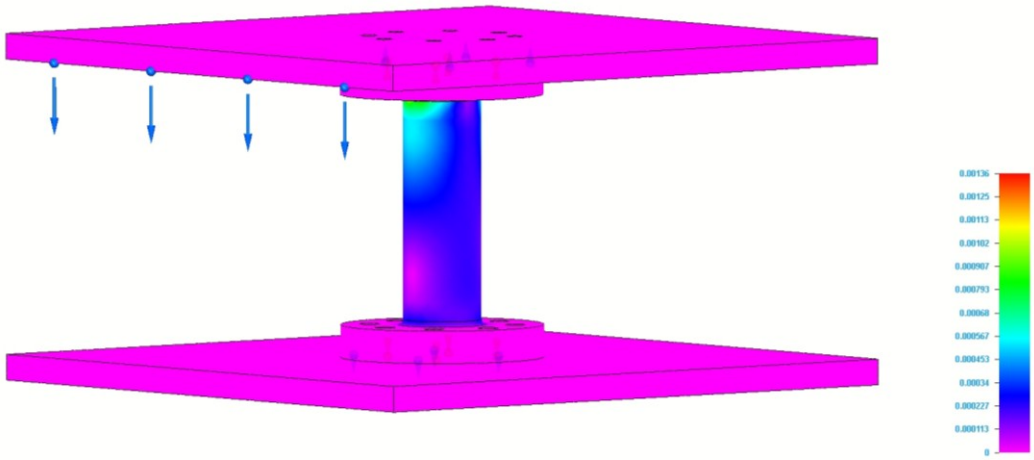

Figure 11:Parallel Surface Loading Condition for Elongated Pylon.

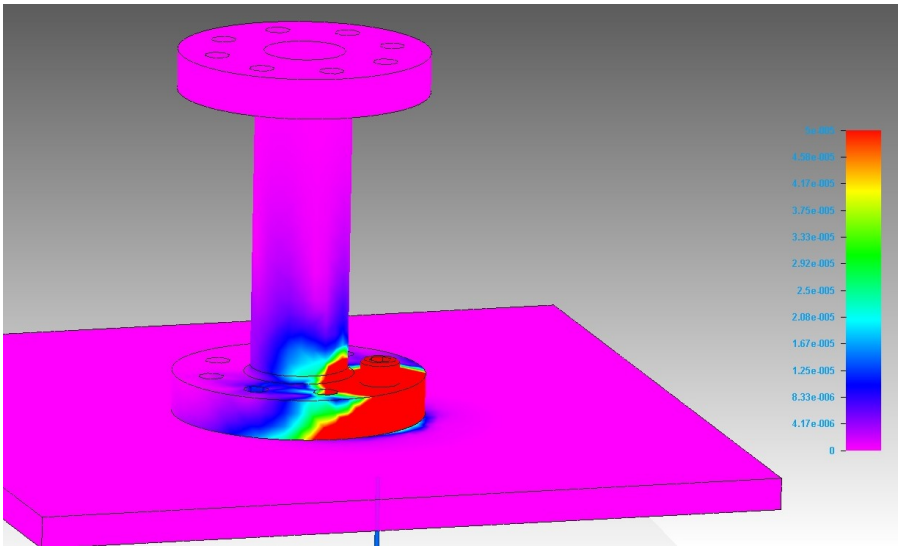

Figure 12: Screw Loading Condition for Elongated Pylon.

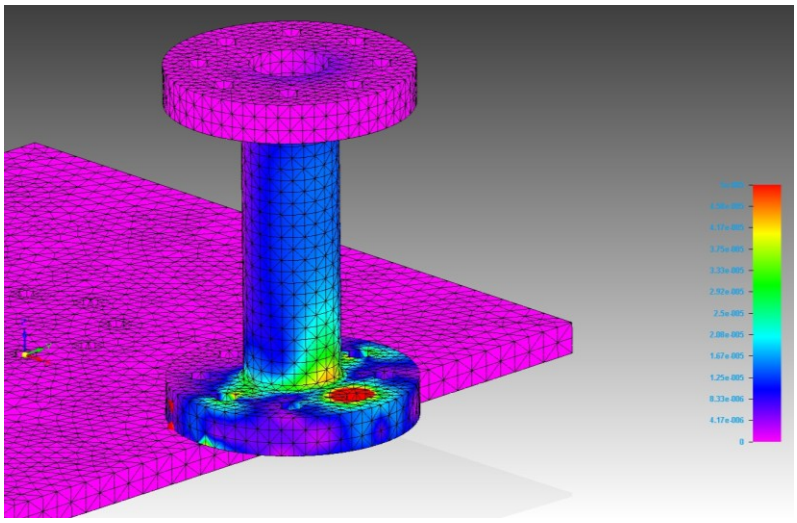

Figure 13: Localized Pylon Deformation for Elongated Pylon.

The next design alteration evaluated a pylon that included a pair of additional rib supports on the pylon shaft. This pylon was also slightly taller than the original pylon design to include the support ribs. The purpose of the support ribs was to ensure that the pylon maintained it original stiffness and natural frequency, but allowed the mounting flanges to be more isolated from gaged section of the pylon. Additionally, unlike the pylon with the elongated shaft, the support ribs prevent the pylon from loss of circularity under higher strain levels at the gaged section. The results of the FEM simulation for this pylon design are shown in figures Figure 14 for the non-parallel surfaces, Figure 15 for the screw preload condition, and Figure 16 for the localized pylon flange deformation. The results confirm that this design modification would reduce the strain at the gaged area of the pylon from the 45με on the original pylon to less than 10με for the pylon with support ribs. The strain seen at the gaged section for the screw preload condition was

reduced to less than 10με, while a strain of 500με was still seen for the non-parallel loading condition.

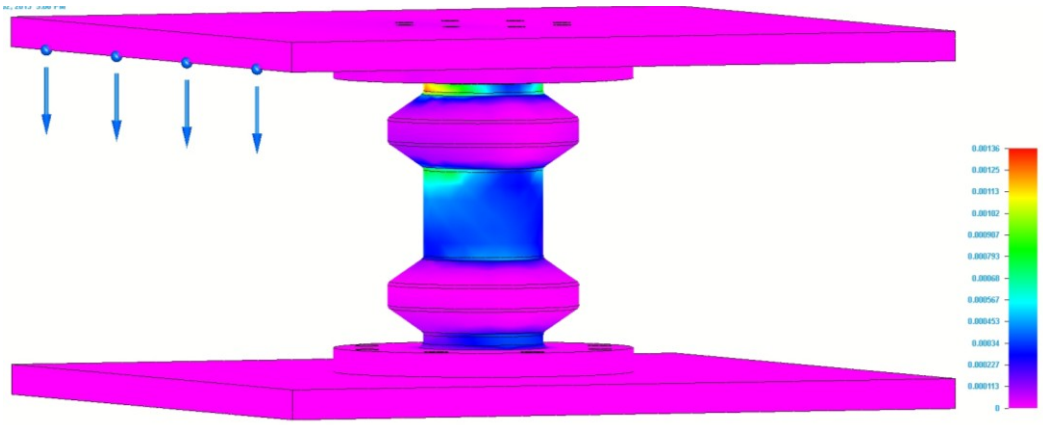

Figure 14: Non-Parallel Loading Condition for Ribbed Pylon Design.

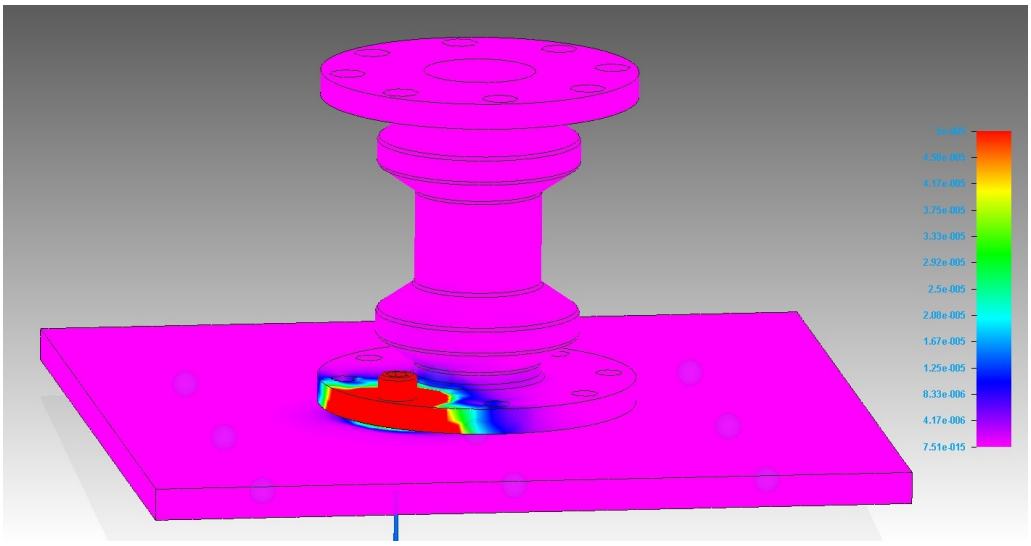

Figure 15: Screw Loading Condition for Ribbed Pylon Design.

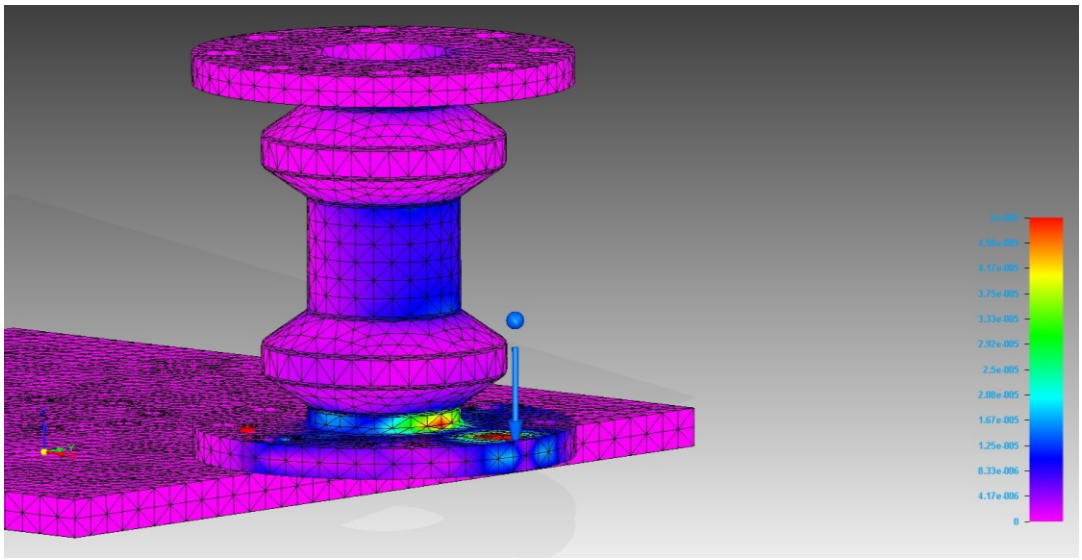

Figure 16: Localized Pylon Flange Deformation for Ribbed Pylon Design.

The third design alteration considered was a thin mounting flange for the pylon. The height of the original pylon was maintained, while the flange thickness on both ends of the pylon was reduced from 0.315” to 0.125”, effectively increasing the length of the pylon shaft an additional 0.38” as well. The goal with the thin mounting flange is twofold. It allows the shaft length to be increased while maintaining the same overall pylon height. Additionally, it makes the mounting flange to be more flexible, allowing it to conform more easily to localized deformation on irregular mounting surfaces and screw clamping preloads while not transferring the strain to the gaged area of the pylon shaft. The results of the three FEM simulations for this pylon design are shown in figures Figure 17 for the non-parallel surfaces, Figure 18 for the screw preload condition, and Figure 19 for the localized pylon flange deformation. The strain levels at the pylon gaged area was reduced only slightly from the original levels of 600με to 550με for the thinner

flange design. For the simulation of the local deformation of the pylon flange, the stain induced at the gaged section of the pylon was reduced from 45με to less than 10με for the thin flange design. Finally, the screw preload loading condition resulted in a significant strain reduction in the gaged section from the original level of 30με to less than 4με.

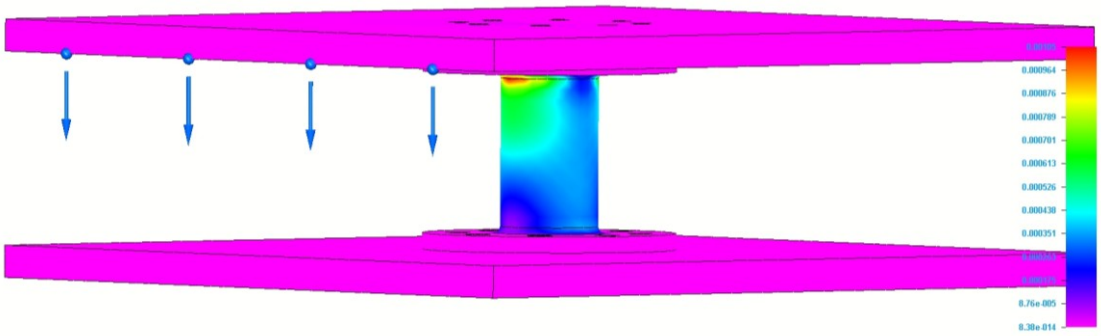

Figure 17: Non-Parallel Mounting Conditions for Thin Flanged Pylon Design.

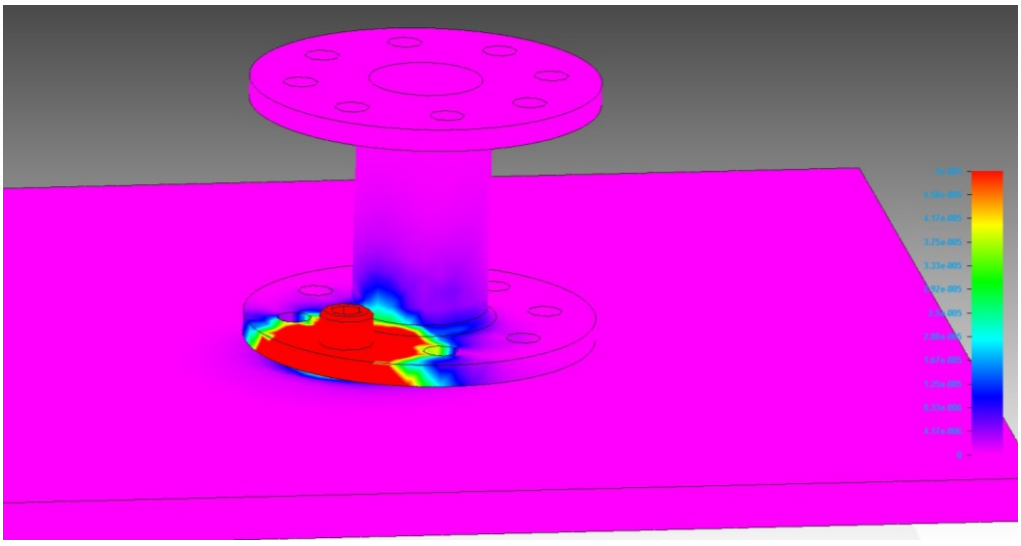

Figure 18: Screw Loading Condition for Thin Flanged Pylon Design.

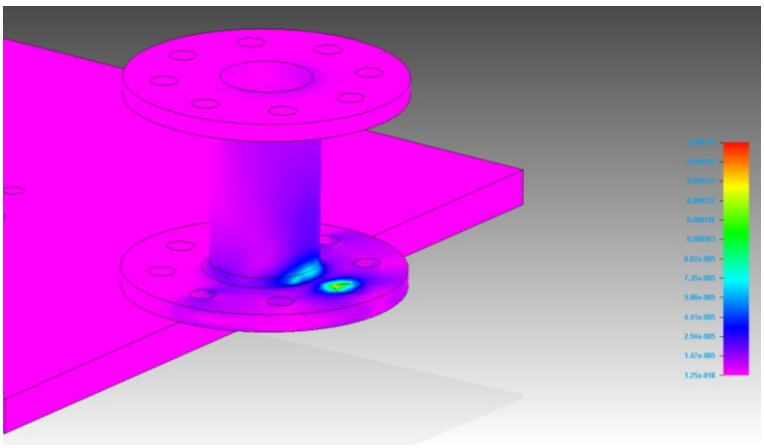

Figure 19: Localized Flange Deformation for Thin Flanged Pylon Design.

The next design feature evaluated was pylon mounting flange diameter. The original pylon was modified to have a mounting flange increased in diameter from 1.97”to 3”, while maintaining the flange thickness and pylon shaft dimensions. By moving screw mounting holes farther from the shaft of the pylon, the strain produced in the gaged section of the pylon by the screw preload should be reduced. The results of the three FEM simulations for this pylon design are shown in Figure 20 for the non-parallel surfaces, Figure 21 for the screw preload condition, and Figure 22 for the localized pylon flange deformation. For the non-parallel surface mounting condition the strain at the gaged section of pylon shaft was 600με, which is unchanged from the original pylon design. The localized pylon flange deformation resulted in strain levels of less than 15με at the gaged section of the pylon, reduced from the 45με or the original pylon design. Finally, the strain at the gaged section of the pylon shaft due to the screw preload was reduced from the 30με of the original pylon design to less than 1με for this increased pylon diameter design.

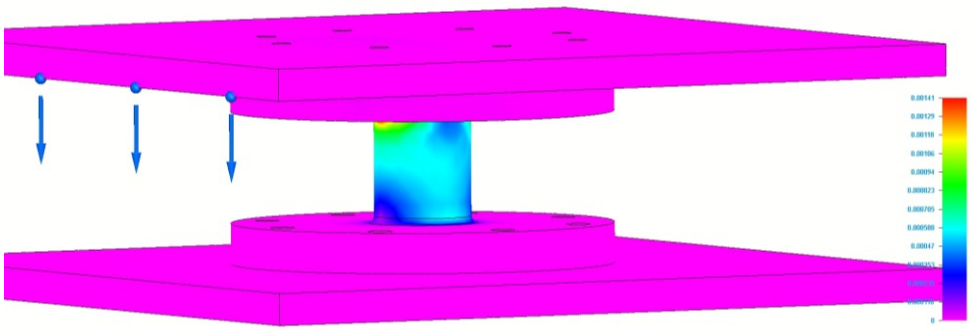

Figure 20: Non-Parallel Loading Condition for Large Diameter Flange Pylon Design.

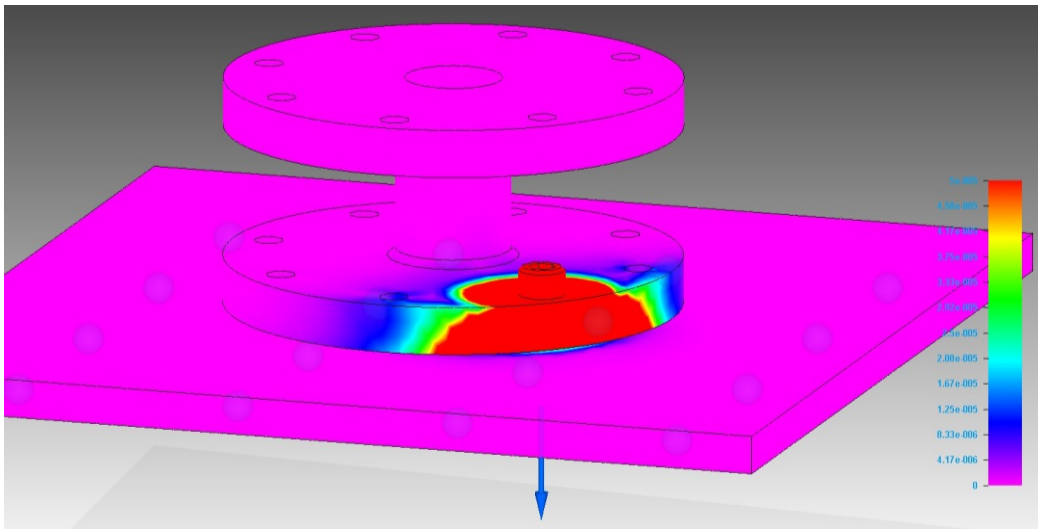

Figure 21: Screw Loading Condition for Large Diameter Flange Pylon Design.

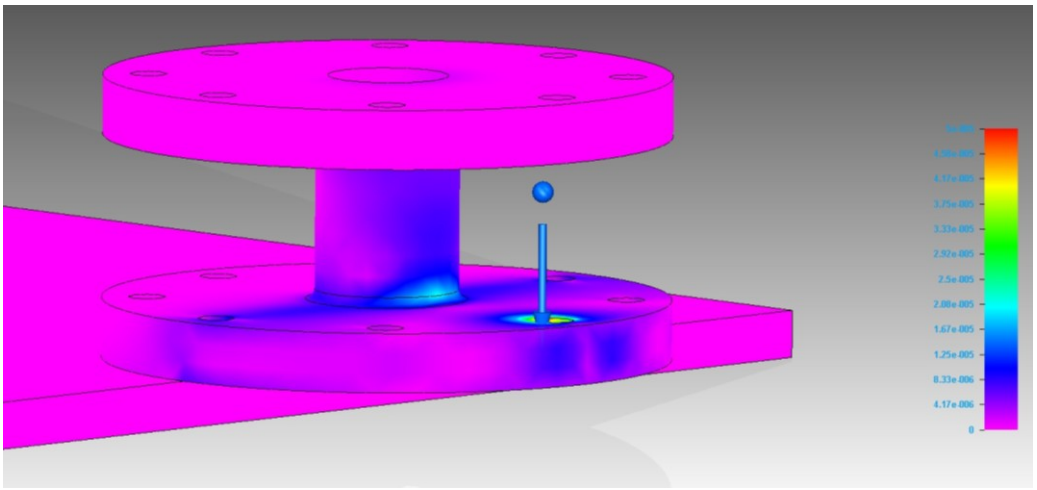

Figure 22: Localized Pylon Flange Deformation for Large Diameter Flange Design.

The next pylon design modification was to determine what effect the pylon shaft diameter has on the resulting strains observed at the gaged area of the pylon. All pylon dimensions were left unchanged from the original pylon, with the exception of the shaft diameter. The outer diameter of the shaft was increased from 0.71" to 1.0", while the wall thickness of the shaft remained unaltered at 0.060". By increasing the diameter to height ratio of the pylon, this design modification would increase the shear stiffness of the pylon, and the resulting shear natural frequency. The results of the three FEM simulations for this pylon design are shown in figures Figure 23 for the non-parallel surfaces, Figure 24 for the screw preload condition, and Figure 25 for the localized pylon flange deformation. The increased shaft diameter of the pylon resulted of strains at the gaged area of the pylon approaching 70με for the localized pylon deformation loading condition, while the screw preload and non-parallel loading conditions resulted in 120με

and 800 με respectively. In each loading condition, the increase in pylon shaft diameter resulted in an increase in strain observed at the gaged area of the pylon.

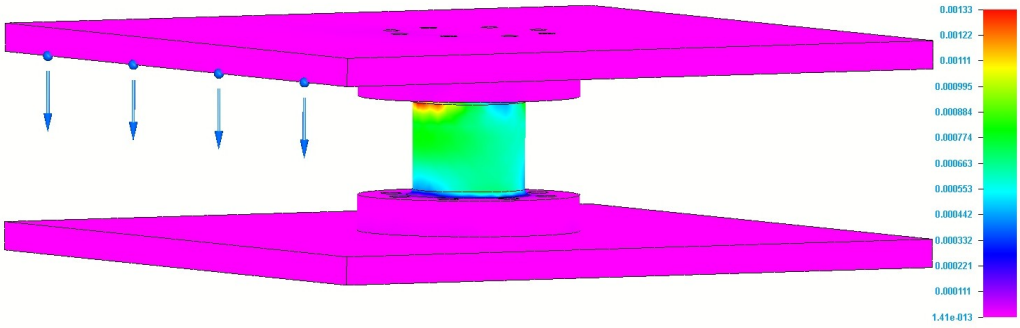

Figure 23: Non-Parallel Surface Condition for Large Diameter Shaft Pylon Design.

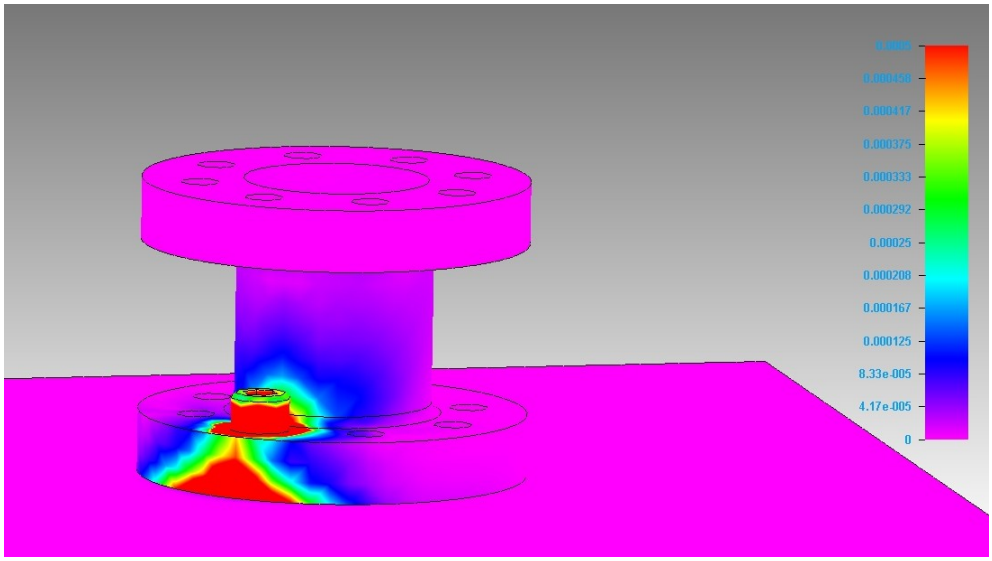

Figure 24: Screw Loading Condition for Large Diameter Shaft Pylon Design.

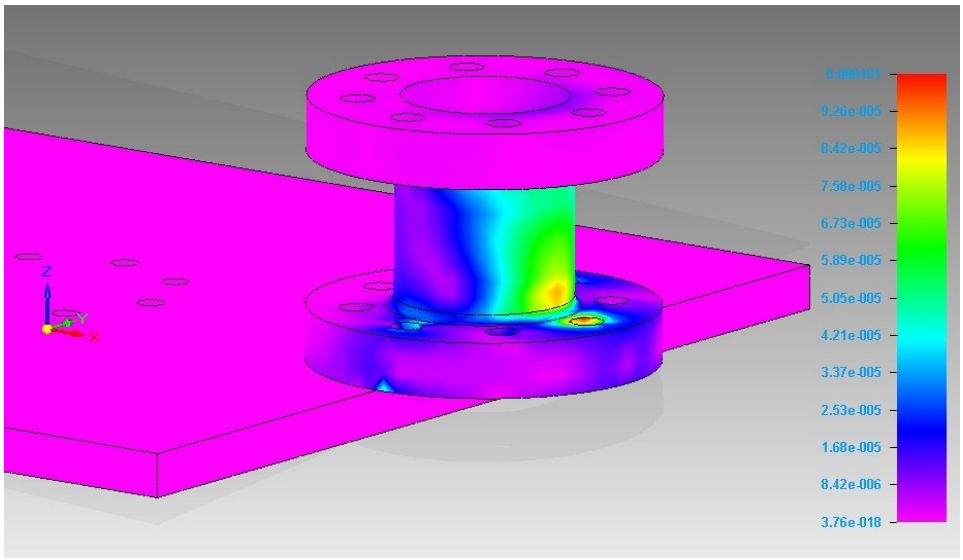

Figure 25: Localized Pylon Deformation for Large Diameter Shaft Pylon Design.

Another pylon design modification tested was a reduction in the inside of the tube diameter. This design modification, shown in Figure 26, includes a 0.5” step on the inside of the pylon that reduces the diameter of the through holes from 0.64” to 0.276”. The results of the three FEM simulations for this pylon design are shown in figures Figure 27 for the non-parallel surfaces, Figure 28 for the screw preload condition, and Figure 29 for the localized pylon flange deformation. The simulation results for the non-parallel loading condition for the reduced inner diameter of the pylon no significant change between the original design, with the strain levels at the gaged section of the pylon still in the range of600με. The simulation results of the localized pylon deformation also showed little changed from the original pylon, with the strain levels at the gaged area decreasing from 45με to 40με. However, the simulation results for the screw preload condition

showed that the reduction in the inside diameter of the pylon does reduce the strains seen at the gaged section significantly from 30με to less than 8με for that loading condition.

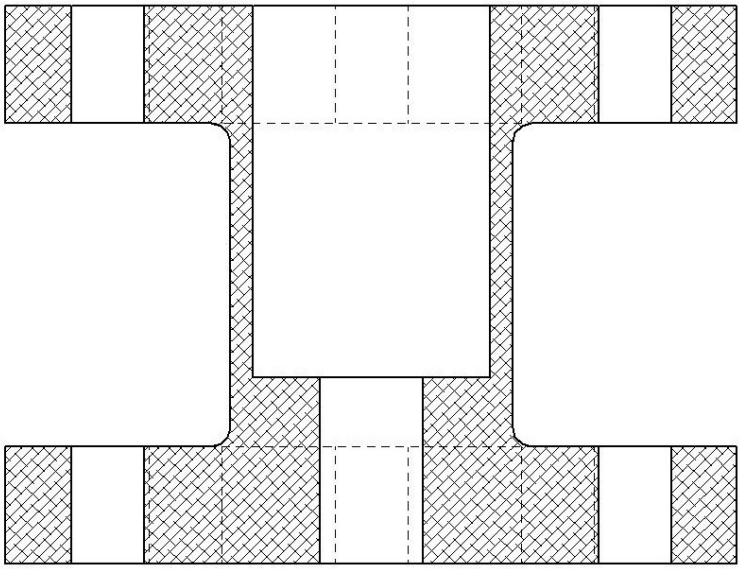

Figure 26: Cross-Section of Inner Diameter Step Pylon Design

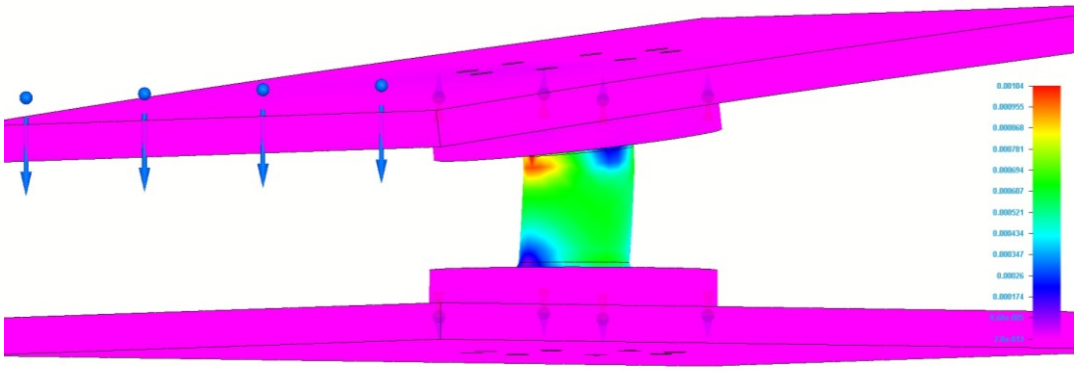

Figure 27: Non-Parallel Surface Condition for Inner Diameter Step Pylon Design.

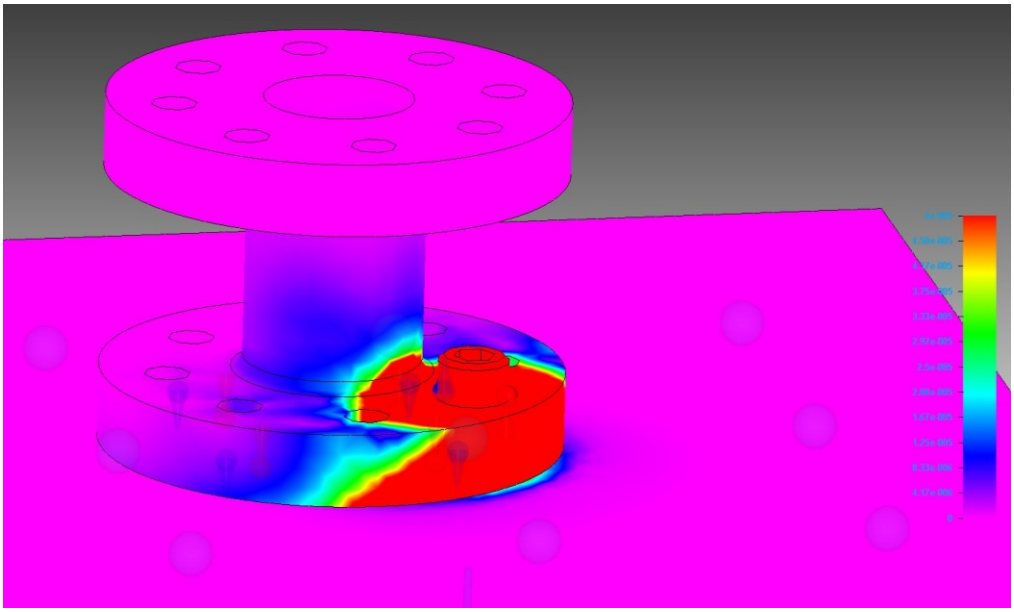

Figure 28: Screw Preload Condition for Inner Diameter Step Pylon Design.

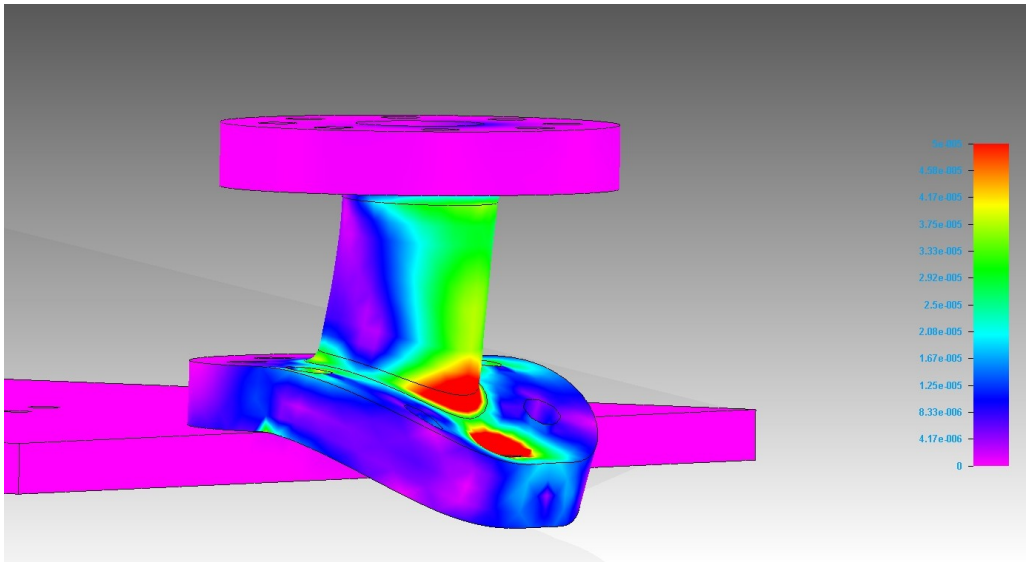

Figure 29: Localized Flange Deformation for Inner Diameter Step Pylon Design.

The final design feature investigated was a potential single mounting bolt through the center of the pylon. This design alteration uses a larger single 7/16" bolt mounting inside the pylon on an internal mounting flange. This pylon design maintains dimensions identical to the original pylon design for the shaft and unaltered mounting flange. This design concept was intended to reduce the effect of irregular and non-parallel surfaces by reducing the surface area of the pylon mounting flange and centering the mounting load. The results of the three FEM simulations for this pylon design are shown in figures Figure 30for the non-parallel surfaces, Figure 31 for the screw preload condition, and Figure 32for the localized pylon flange deformation. The FEM simulation results for the non-parallel surface loading condition show the strain levels at the gaged area of the pylon were reduced from 600με to 500με, while the results of the localized pylon flange deformation showed a decrease in strain levels from 45με to less than 10με. The strain induced in the gaged area of the pylon due to the screw preload was determined with a

different loading condition than previous design modifications. Rather than applying the load to a single #10 screw, an 11830 lb clamping load resulting from an 1190 in-lb torque was applied to the single 7/16" screw. This loading condition resulting in strains at the gaged section of nearly 800με, which is a far more significant than the loading resulting from the original #10 mounting screws.

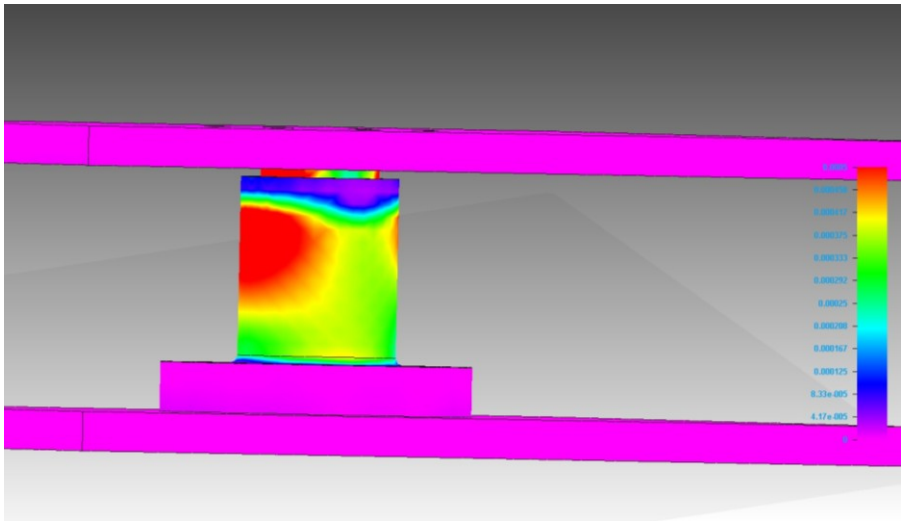

Figure 30: Non-Parallel Surface Loading Condition for Single Bolt Design.

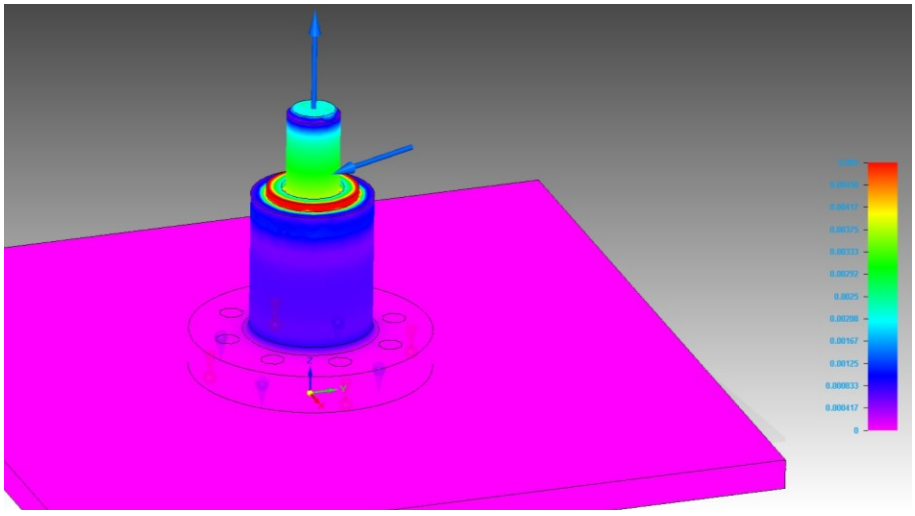

Figure 31: Screw Loading Condition for Single Bolt Design

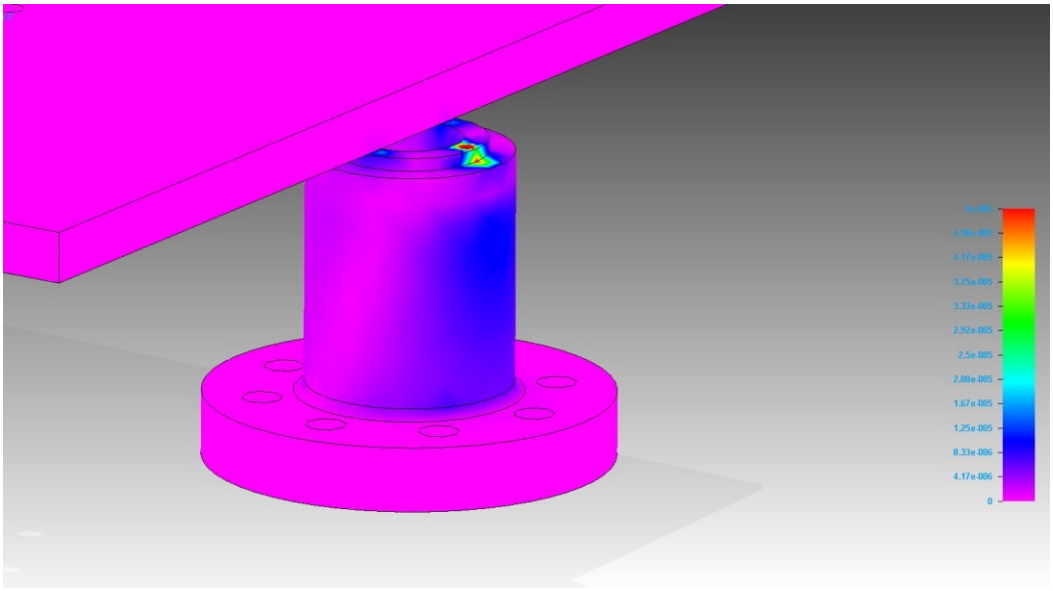

Figure 32: Localized Flange Deformation for Single Screw Mount Pylon Design.

2.3: Design Selection

Based on the FEM simulation results from these simulations, several conclusions can be made about which geometries best isolate the gaged area of the pylon from the variability in the mounting conditions of the pylon. Of the 6 design alteration tested, the long pylon shaft design had a significantly larger reduction in the strain due to the non-parallel surface loading condition. However, implementing an elongated shaft into a force platform design has several drawbacks that the current pylon do not have. Firstly, increasing the length of the pylon increases the overall height of the platform, requiring more space to mount the device in either a pit or raised floor structure. Secondly, increasing the pylon shaft length without increasing the wall thickness or diameter will decrease the systems overall shear stiffness, resulting in a lower overall natural frequency, and potentially leading to undesirable noise that will require data filtering. Of

remaining 5 test designs, the rib support, thin flange, and single bolt design all result in minor reductions of the strain due to the non-parallel loading condition. However, the single bolt design results in a drastic increase in strain at the gaged section due to the clamping load of the larger diameter screw in close proximity to the gaged area. Therefore the rib support and thin flange designs appear to be the best design to reduce the effects of the non-parallel loading condition on the pylons. The effects of the local deformation of the pylon mounting flange were most significantly reduced by the rib support, thin flange, and single bolt design, although the elongated and large diameter flange also showed significant reductions. The strain caused by the screw preload was most significantly reduced by the rib support, thin flange, and large diameter flange designs. Based on the results of all three loading simulations, the rib support design and thin mounting flange design proved to be most effective at isolating the pylon gaged area from the pylon boundary conditions, without significant drawbacks to the overall force platform design.

The first prototype design involved a combination of elements tested in the FEM simulations. Unlike previous pylon designs which utilize a single aluminum tube structure, the new pylon design consists of 3 separate structures. The central pylon piece remains unchanged as an aluminum tube with mounting flanges on both ends. However, each side of the pylon now has an attached stainless steel flanged spacer. The attachment of the stainless steel spacers allows the aluminum pylon geometry to remain relatively unchanged, while still incorporating several of the effective design elements identified with the FEM simulations. The outermost flange of the stainless steel spacer has a

thickness of only 1/8", allowing the flange to conform to the mounting surface and reduce strain due to the screw preloads. Additionally, the mounting flange and hole pattern are a significantly larger diameter than the original pylon design, further isolating the gaged area of the pylon from the boundary conditions of the mounting surfaces. The stainless steel spacer also has a second thicker mounting flange that connects the spacer to the aluminum pylon part. The second flange is designed to act much like the support ribs for isolating the gaged area from the mounting condition. Additionally, the through hole is a smaller diameter than inner aluminum pylon, similar in geometry to the smaller inner diameter step tested in the simulations. Stainless steel was selected for the spacer material because it provides a much higher stiffness, 28000 ksi, in comparison to the aluminum 6061-T6 used for the central pylon which has a modulus of elasticity of only 10000 ksi. The increased stiffness allows the pylon height to increase slightly without greatly reducing the overall natural frequency of the force platform.

The prototype pylon design was evaluated using the same loading conditions previously tested in the FEM simulations. When tested with the non-parallel surface loading condition, the prototype pylon showed strain levels around 500με, which is a reduction of 15% from the original pylon design, as shown in Figure 33. When the pylon was evaluated using the screw preload condition, the loading was effectively isolated for the prototype design, as shown in Figure 34, with the strain levels at the gaged area of the pylon reduced to negligible levels. When the localized pylon deformation condition was simulated as shown in Figure 35, the gaged area of the pylon experienced only 5με of strain, a 92% decrease from the original pylon design, and a

significant improvement over any of the previously tested design features. These FEM simulations confirmed that the prototype design should be able to effectively reduce strain levels at the gaged area due to adverse mounting conditions during force platform assembly and installation.

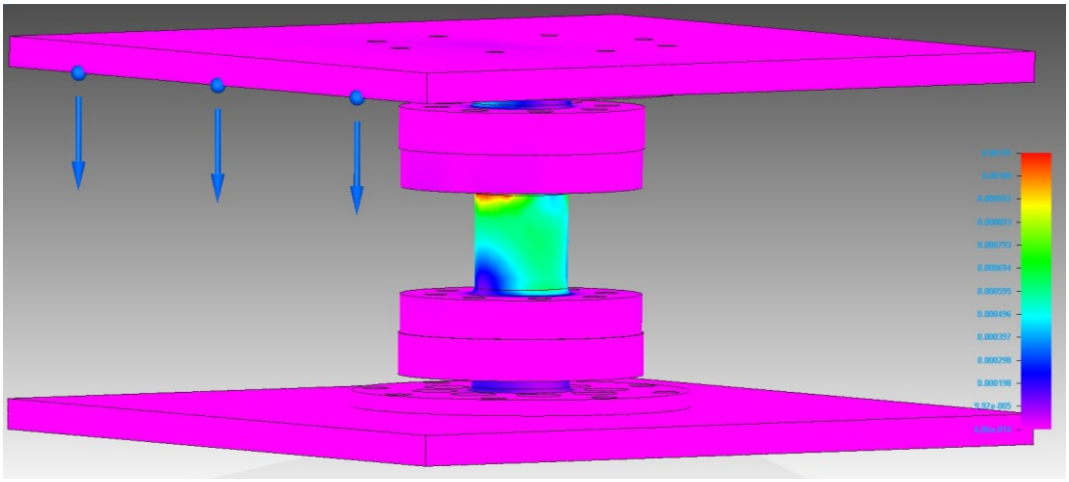

Figure 33: Non-parallel Loading Condition for First Prototype Pylon Design.

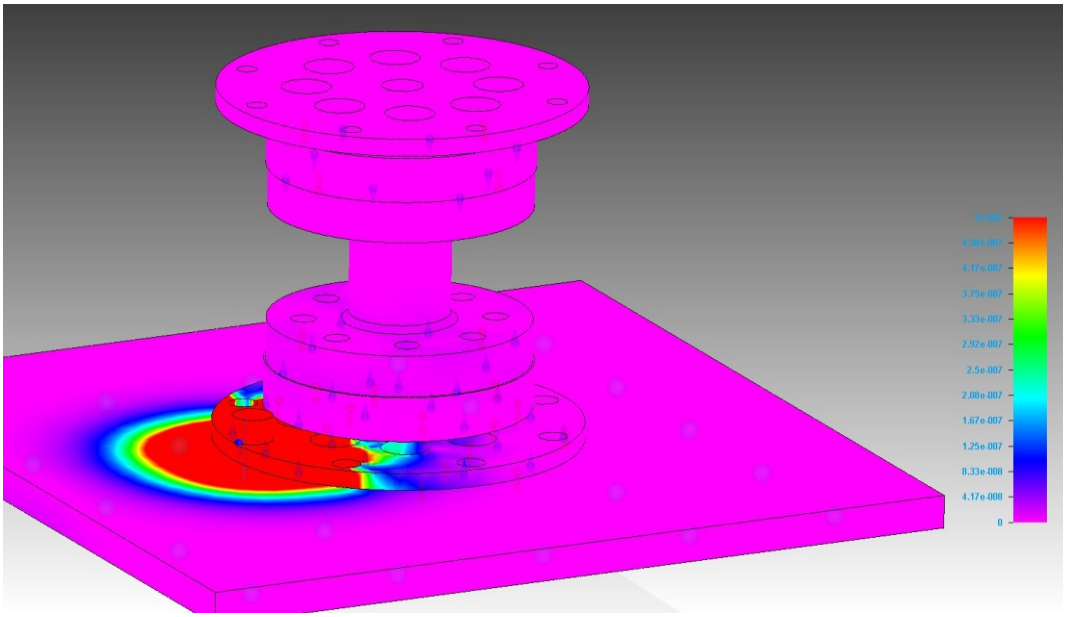

Figure 34: Screw Loading Condition for First Prototype Design.

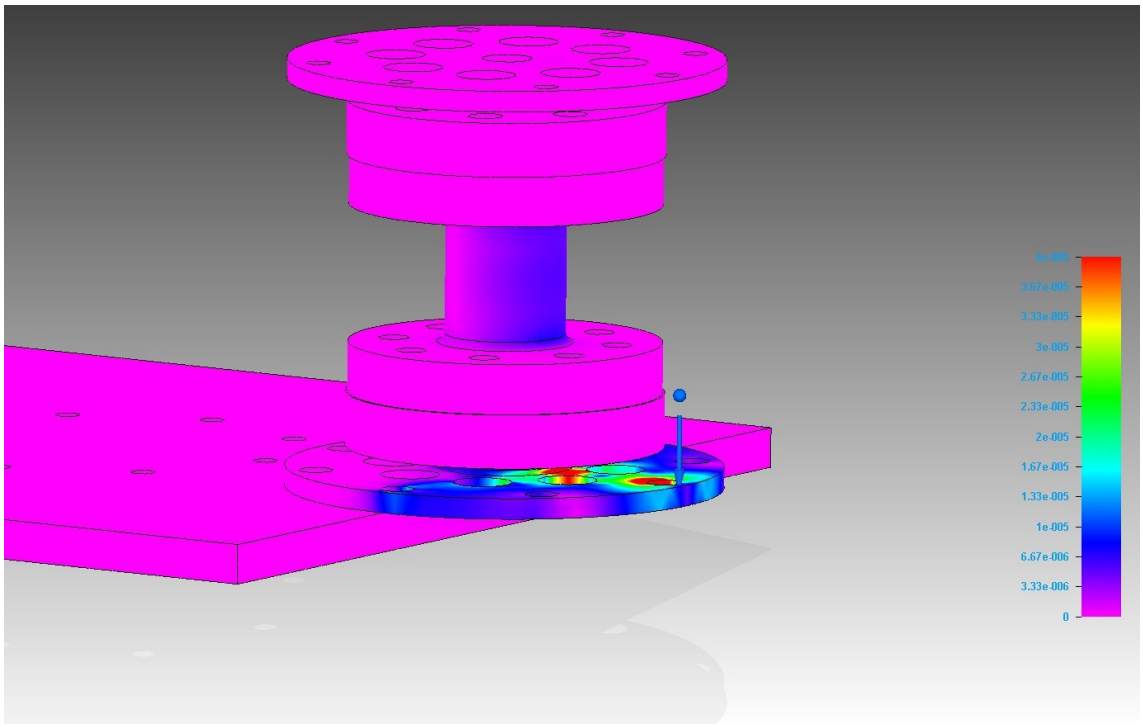

Figure 35: Localized Flange Deformation for First Prototype Design.

A second prototype design was also tested using the FEM software. This second design used the same stainless steel spacers as the first prototype design, but also used a modified aluminum pylon. The modified aluminum pylon, shown in Figure 36next to the original pylon, had an increased outer shaft diameter of 1.0", a mounting flange thickness decreased from 0.315" to 0.2", and a shaft length decreased from 0.875" to 0.625".

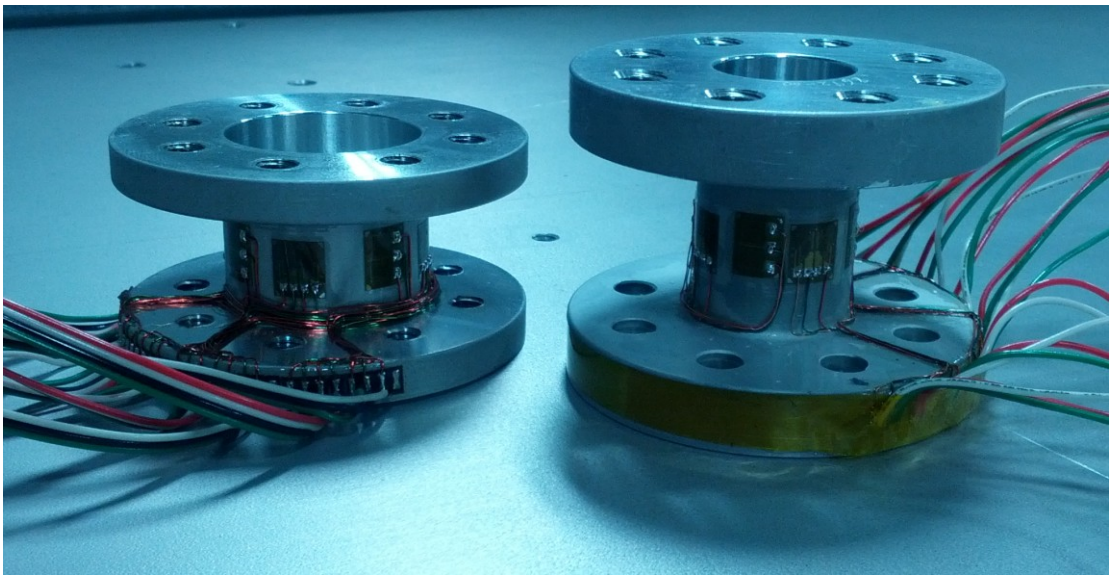

Figure 36: Modified Aluminum Pylon (Left) and Original Aluminum Pylon (Right)

This design was tested using the FEM software under the same loading conditions as the first prototype. The resulting strains at the gage mounting location for the screw preload and local flange deformation, shown in Figure 37and Figure 38, were very similar to the results for the first pylon prototype design. The maximum strain at the gage section due to the screw preload was less than 1με, while the local flange deformation caused a strain of 10με. The second prototype design performed poorly, however, in the non-parallel surface loading condition. The resulting simulation, shown in Figure 39, showed that the design actually resulting in a higher strain at the gaged area of the pylon that other previously designs, reaching levels as high as 750με at the gaged section.

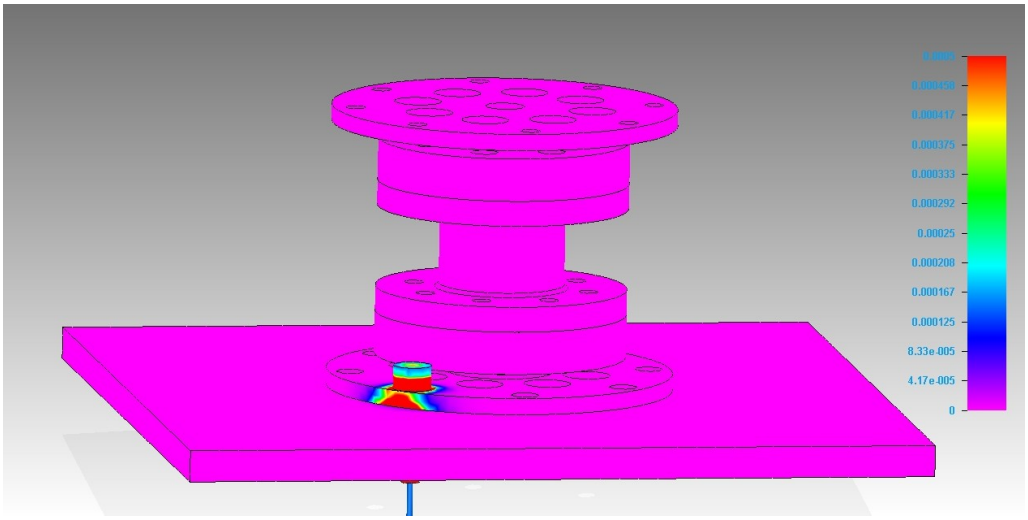

Figure 37: Screw Loading Condition for Second Pylon Prototype.

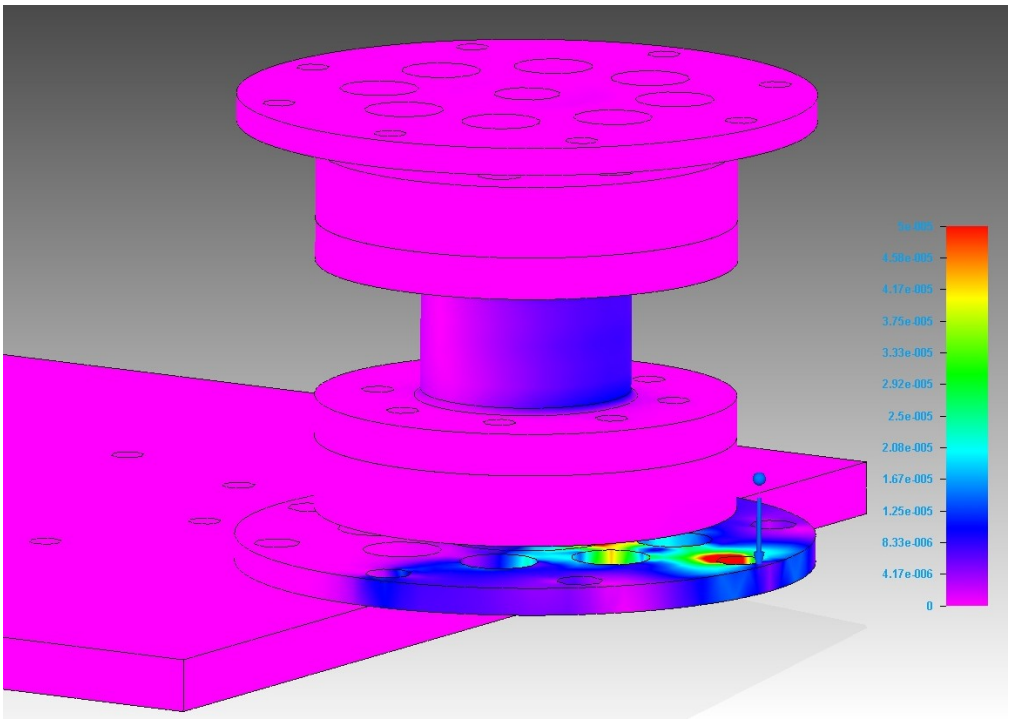

Figure 38: Localized Pylon Deformation for Second Prototype Pylon.

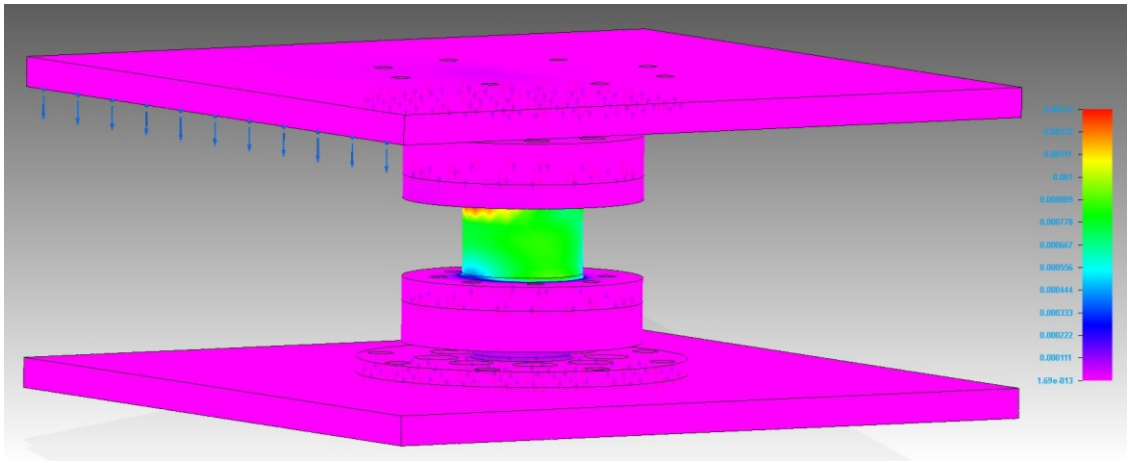

Figure 39: Non-parallel Loading Condition for Second Prototype Pylon

This result is expected, considering the decreased length of the aluminum portion of the pylon, as well as the increased diameter to height ratio of the pylon. Despite the second prototype performance in the non-parallel surface condition simulation, it has the additional advantage of being shorter than the first prototype, as well as having higher shear stiffness due to the increased outer diameter of the pylon shaft. This increased shear stiffness was a sufficient added benefit to at least warrant physical testing.

Chapter 3: Results and Testing

In order to verify that the prototype pylons were effective at isolating the strain gages from the pylon boundary conditions of the load cell, it was then necessary to manufacture, gage, calibrate, and test the pylons. Two sets of four pylons and stainless steel spacers were manufactured for testing so that their performance in assembled force platform could be evaluated. The machined stainless steel spacers are shown in Figure 40, while Figure 41shows the first prototype pylon completely assembled with the stainless steel spacers before the initial calibration. The second prototype pylon with a larger shaft diameter is shown assembled with the stainless steel spacers in Figure 42.

Figure 40: Stainless Steel Spacers for Prototype Pylon Design.

Figure 41: First Prototype Pylon Design Assembly.

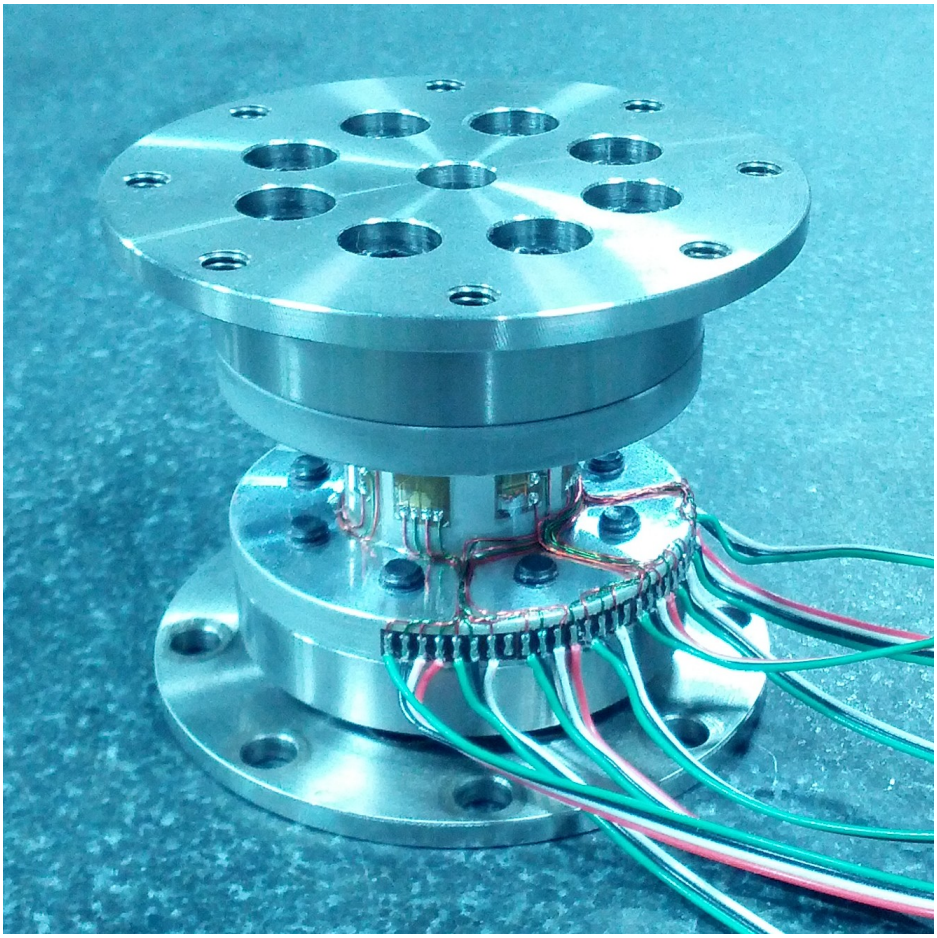

Figure 42: Second Prototype Pylon Design Assembly.

Once each prototype pylon was assembled, the next step was to calibrate the load cell. However, due to the change from 3-component load cells to 6-component load cells, several changes needed to be made to the calibration process. Previously, 3-component load cells were first assembled into the force platform and then the platform unit was calibrated by applying deadweights at several key points along the top surface of the

force platform. With the change to the 6-component pylons, the calibration process requires that each load cell be calibrated independently. Calibrating pylons individually introduces several complications to the process. Independent calibration of the pylon removes the physical constraint on one end of the pylon by removing the other 3 pylons and mounting plate. The removal of this constraint allows one end of the pylon to move freely when a load is applied to it, which is unlike the loading conditions it experiences when assembled in the force platform between two surfaces. In order to compensate for the cantilever end of the pylon, a calibration system was devised to more closely resemble the loading conditions that the pylon will see in the assembled force platform. The calibration plate, shown in Figure 43, consists of an aluminum block mounted on the cantilever end of the pylon, which in turn is attached to a parallel aluminum plate which intersects the midline of the pylon, so that the shear forces do not apply a significant moment during calibration.

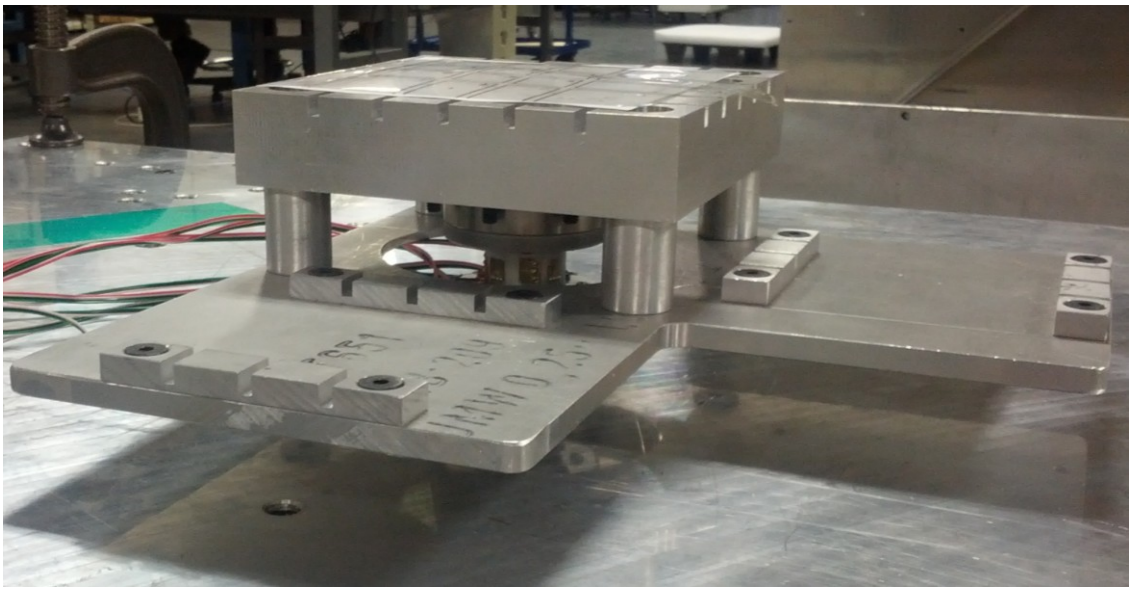

Figure 43: First Prototype Pylon with Assembled Calibration Plate.

The calibration plate allows for a total of 27 calibration data points to be taken for each pylon. First, 9 data points are taken by applying a vertical load with deadweights to a 3 x 3 pattern of equally spaced marks 1.5” apart on the top plate of the pylon. Next, the same vertical load are again applied to the same 9 points with the addition of a shear loads applied x axis at the midline of the pylon. The shear load was applied using a cable, hook, pulley, and deadweight, as shown in Figure 44.

Figure 44: Calibration Plate Setup with Vertical and Shear Calibration Weights Applied.

By applying the shear load at the midline of the pylon, the free end of the pylon is kept parallel to the fixed end during deformation, maintaining the geometric constraints similar to what the pylon will experience when both ends are fixed between two parallel plates. The model in Figure 45 shows the pylon deformation when a shear load is applied at the top of a cantilever pylon, Figure 46 shows the model when the shear load is applied at the midline of a pylon using an addition calibration plate, while Figure 47 shows the pylon deformation when the shear load is applied to two parallel mounting plates similar to the actual treadmill loading conditions.

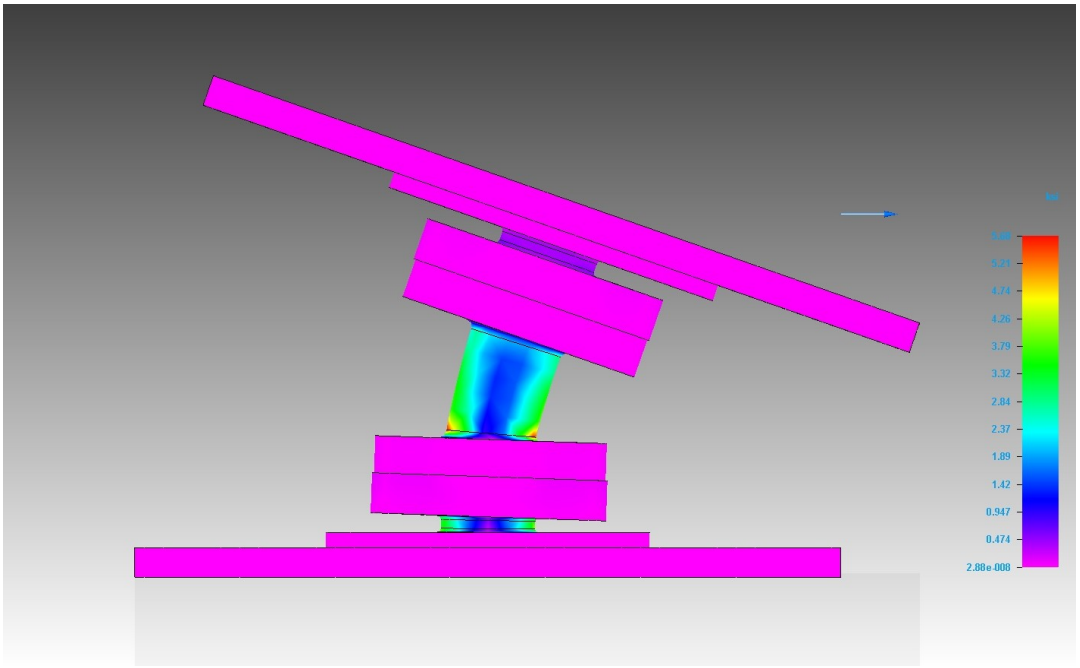

Figure 45: Pylon Deformation Due to Cantilever Loading.

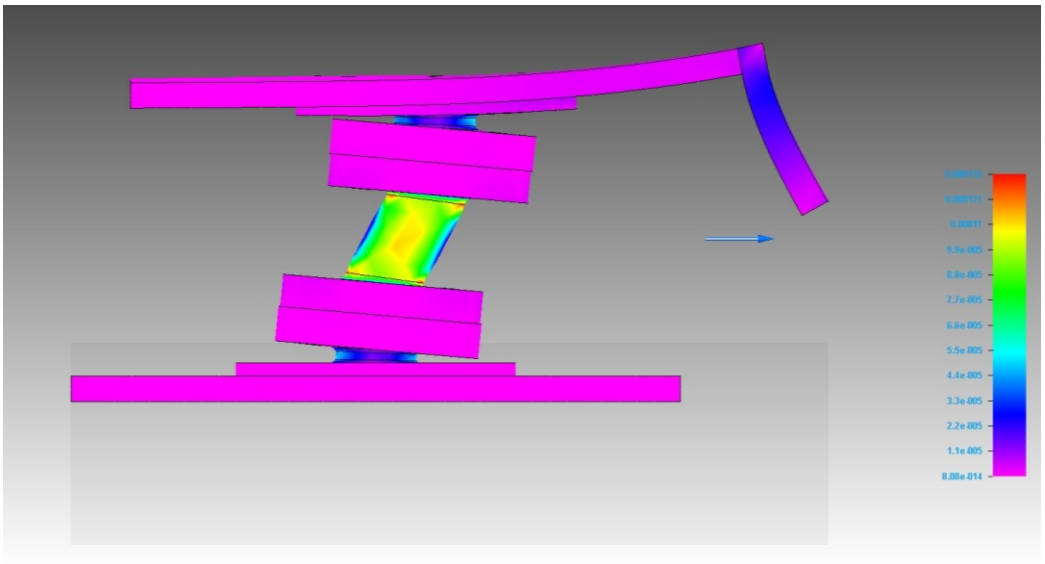

Figure 46: Pylon Deformation Due to Loading at the Pylon Midline.

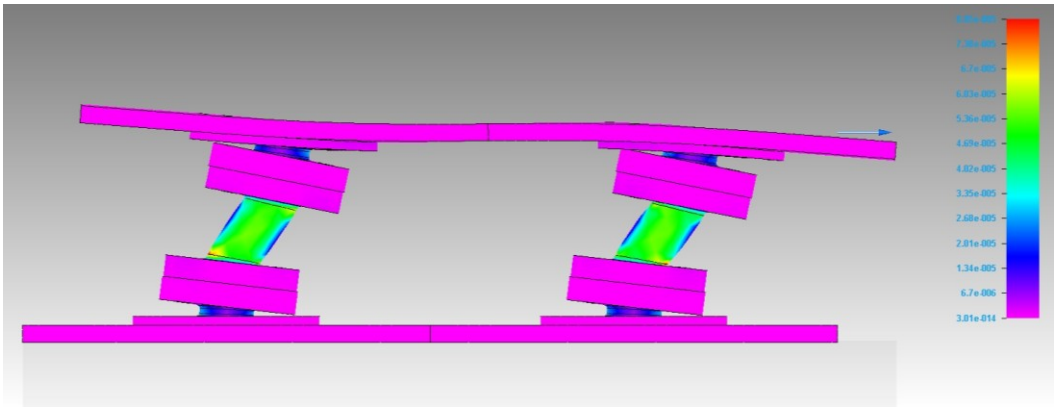

Figure 47: Pylon Deformation Due to Displacement of Parallel Plates.

Finally, another 9 combined vertical and shear data points were collected, this time by applying the shear loads in parallel to the y axis at the midline of the pylon. The matrix of 27 data points was then fit to the known applied loads by using a Moore-Penrose pseudo inverse of the matrix. The best fit from the inverse matrix is used as the "calibration matrix" to convert the voltage signals from the strain gages to uses load signals. An additional "error matrix" is produced from each calibration matrix, indicating the error from the known applied load at each of the 27 calibration points. For individual 6-component pylons, deviation levels under 2 N are low enough to meet internal Bertec accuracy standards. Table 1, Table 2, and Table 3 show the error matrices for the first set of prototype pylons, while the error matrices for the second set of prototype pylons are shown in Table 4, Table 5, and Table 6.

Table 1: First Prototype Pylon Calibration Error (N) for Points 1-9 (Vertical Loading).

	Load	Point 1	Point 2	Point 3	Point 4	Point 5	Point 6	Point 7	Point 8	Point 9
Pylon A	F_x	-0.25	-0.10	0.13	0.14	0.17	0.00	0.11	-0.05	-0.18
	F_y	0.04	0.15	0.05	0.01	0.11	-0.11	-0.07	-0.11	-0.07
	F_z	-0.39	0.04	0.18	0.04	0.26	0.22	-0.22	0.42	-0.56
	M_z	-0.03	-0.05	-0.01	0.10	0.05	-0.09	-0.03	0.00	0.05
	M_y	-0.15	-0.02	0.04	0.04	0.00	0.04	0.11	-0.06	0.00
	M_z	0.02	-0.01	-0.01	0.02	0.00	-0.01	0.01	-0.01	-0.01
Pylon B	F_x	-0.06	0.15	0.00	-0.07	0.04	0.07	-0.02	0.06	-0.19
	F_y	0.09	-0.12	0.08	0.09	0.11	0.09	-0.20	-0.12	-0.01
	F_z	-0.54	-0.01	-0.28	-0.05	0.88	0.21	-0.56	0.67	-0.37
	M_z	0.03	-0.04	0.09	0.02	-0.13	0.02	0.07	-0.01	-0.05
	M_y	-0.04	-0.09	-0.03	0.07	0.17	0.07	-0.07	-0.15	0.07
	M_z	-0.01	0.00	0.00	-0.01	-0.01	0.00	0.01	0.00	0.00
Pylon C	F_x	0.22	0.07	0.23	0.00	0.10	-0.11	-0.03	-0.27	-0.23
	F_y	-0.35	0.05	0.14	-0.27	-0.31	0.30	0.37	0.15	-0.07
	F_z	-0.47	0.29	-0.73	0.02	1.13	0.65	-0.83	0.47	-0.57
	M_z	0.04	-0.04	0.05	-0.11	0.00	0.00	0.06	-0.06	0.06
	M_y	0.11	0.01	-0.03	0.06	-0.05	0.06	-0.05	-0.05	-0.06
	M_z	0.01	0.00	0.00	0.03	-0.01	-0.01	0.00	0.00	-0.02
Pylon D	F_x	-0.07	0.16	-0.18	0.36	0.01	-0.26	0.15	-0.03	-0.14
	F_y	-0.31	-0.12	0.33	0.03	0.20	-0.05	-0.25	0.18	-0.01
	F_z	-0.07	0.04	-0.43	-0.52	0.93	0.60	-0.51	0.16	-0.20
	M_z	0.05	0.02	-0.08	-0.03	0.01	0.02	0.05	-0.05	0.01
	M_y	-0.03	0.07	-0.08	0.07	0.02	0.00	-0.05	0.03	-0.03
	M_z	0.01	0.00	0.01	0.00	0.00	0.00	0.00	0.00	-0.01

Table 2: First Prototype Pylon Calibration Error (N) for Points 10-18 (X-Axis Shear and Vertical Loading).

	Load	Point 10	Point 11	Point 12	Point 13	Point 14	Point 15	Point 16	Point 17	Point 18
Pylon A	F_x	0.28	0.43	-0.04	-0.57	-0.46	-0.41	0.48	-0.09	0.41
	F_y	-0.10	-0.01	-0.21	0.07	-0.10	0.28	-0.08	0.25	-0.10
	F_z	-0.43	0.15	0.11	-0.16	0.75	-0.22	-0.17	0.35	-0.40
	M_z	0.10	0.04	0.02	-0.07	-0.16	0.00	-0.01	0.08	-0.01
	M_y	0.05	0.03	-0.04	0.00	0.03	0.06	-0.07	0.00	-0.06
	M_z	0.00	0.01	0.02	-0.02	0.01	0.02	-0.03	-0.01	-0.01
Pylon B	F_x	0.09	0.06	0.02	0.00	-0.26	0.12	-0.10	-0.24	0.32
	F_y	0.02	-0.25	0.39	0.08	-0.52	-0.38	0.38	-0.18	0.46
	F_z	0.34	0.15	-0.22	-0.47	0.37	0.00	-0.20	0.30	-0.27
	M_z	-0.04	-0.04	0.04	0.03	0.13	0.02	-0.03	-0.12	0.03
	M_y	0.01	0.00	-0.08	0.00	0.09	0.09	-0.07	0.04	-0.09
	M_z	-0.01	0.01	-0.03	0.00	0.06	0.05	-0.03	0.00	-0.05
Pylon C	F_x	-0.20	0.02	0.33	-0.38	-0.20	-0.12	0.33	0.04	0.20
	F_y	0.46	0.01	-0.11	-0.49	-0.37	-0.15	0.32	0.53	-0.20
	F_z	-0.88	-0.13	-0.08	0.78	1.09	0.46	-0.34	-0.28	-0.64
	M_z	0.04	-0.01	0.03	-0.05	-0.07	-0.09	0.05	0.06	0.04
	M_y	-0.07	-0.09	0.00	0.06	0.10	0.03	-0.03	-0.02	0.03
	M_z	0.00	-0.03	0.03	0.02	0.01	0.04	-0.01	-0.08	0.02
Pylon D	F_x	0.28	0.04	0.38	-0.55	-0.35	0.17	0.37	-0.41	0.09
	F_y	0.15	-0.13	0.08	-0.09	0.06	-0.68	0.20	0.10	0.32
	F_z	-0.18	0.12	0.23	-0.46	1.00	-0.35	-0.49	0.59	-0.48
	M_z	-0.01	0.00	0.02	0.16	-0.13	-0.04	-0.11	0.05	0.05
	M_y	0.04	0.00	0.16	-0.09	0.03	-0.23	-0.03	0.07	0.06
	M_z	-0.01	0.01	-0.01	0.01	-0.01	0.06	-0.03	-0.01	-0.02

Table 3: First Prototype Pylon Calibration Error (N) for Points 19-27 (Y-Axis Shear and Vertical Loading).

	Load	Point 19	Point 20	Point 21	Point 22	Point 23	Point 24	Point 25	Point 26	Point 27
Pylon A	F_x	0.06	0.06	0.16	-0.16	-0.08	-0.06	-0.03	0.04	0.02
	F_y	-0.01	0.15	-0.28	-0.18	0.02	0.32	0.12	-0.08	-0.08
	F_z	-0.18	0.07	-0.41	0.40	0.47	-0.08	-0.51	0.69	-0.45
	M_z	0.03	-0.04	0.00	0.00	0.03	0.00	-0.07	0.02	0.03
	M_y	0.01	0.03	0.01	-0.04	-0.02	-0.02	0.05	0.01	-0.03
	M_z	-0.03	-0.01	-0.01	0.02	0.00	-0.01	0.02	0.01	0.02
Pylon B	F_x	-0.05	-0.02	-0.25	-0.09	0.29	0.01	0.11	0.27	-0.27
	F_y	0.05	-0.23	0.02	0.09	0.35	-0.05	-0.10	-0.03	-0.11
	F_z	-0.22	0.13	-0.33	-0.16	0.76	0.41	-0.11	0.58	-1.05
	M_z	0.01	-0.21	0.15	0.08	0.00	-0.12	0.04	0.07	-0.01
	M_y	-0.03	0.09	0.07	0.01	-0.09	-0.20	0.06	0.03	0.05
	M_z	0.01	-0.01	0.00	0.00	-0.03	-0.01	0.02	-0.01	0.01
Pylon C	F_x	-0.37	0.10	-0.13	0.06	0.21	-0.10	0.73	-0.74	0.23
	F_y	-0.12	0.04	0.09	-0.04	0.47	0.36	0.09	-0.52	-0.40
	F_z	-0.08	-0.36	-0.88	0.07	1.68	0.71	-0.21	-0.14	-0.79
	M_z	0.01	0.03	0.00	-0.02	0.13	-0.10	0.03	-0.14	0.06
	M_y	-0.08	0.08	-0.01	0.05	-0.07	-0.07	-0.03	0.07	0.07
	M_z	0.01	-0.03	-0.01	-0.01	-0.03	-0.01	0.00	0.09	-0.01
Pylon D	F_x	0.04	-0.52	-0.02	0.04	0.02	0.38	-0.10	0.00	0.15
	F_y	0.08	-0.14	-0.04	0.33	0.17	0.27	-0.20	-0.24	-0.25
	F_z	0.17	-0.06	-0.50	-0.21	0.74	-0.29	0.30	0.39	-0.53
	M_z	-0.03	0.10	0.05	-0.03	-0.10	-0.07	-0.01	0.05	0.06
	M_y	-0.06	-0.04	0.02	-0.03	0.06	0.06	0.02	0.06	-0.10
	M_z	-0.01	0.00	-0.02	0.01	0.01	-0.02	0.01	0.02	0.00

Table 4: Second Prototype Pylon Calibration Error (N) for Points 1-9 (Vertical Loading).

	Load	Point 1	Point 2	Point 3	Point 4	Point 5	Point 6	Point 7	Point 8	Point 9
Pylon A	F_x	-0.03	0.02	0.28	0.18	0.14	0.09	-0.07	-0.23	-0.35
	F_y	0.07	0.20	-0.01	-0.08	0.08	0.10	-0.27	0.02	-0.10
	F_z	-0.13	-0.29	-0.01	-0.07	0.19	-0.04	-0.07	0.18	0.24
	M_z	-0.07	-0.03	-0.02	0.04	0.00	0.05	0.00	0.05	-0.02
	M_y	0.08	-0.08	0.00	-0.02	-0.02	-0.01	-0.01	0.04	0.03
	M_z	-0.01	-0.01	-0.02	-0.01	0.00	0.00	0.01	0.02	0.02
Pylon B	F_x	-0.06	0.03	0.05	-0.15	-0.04	0.00	-0.06	-0.11	0.31
	F_y	0.06	-0.15	-0.03	0.15	0.08	0.04	-0.08	0.02	-0.07
	F_z	-0.26	-0.14	0.01	-0.32	0.93	-0.15	0.02	0.06	-0.13
	M_z	-0.03	-0.02	0.04	-0.01	-0.06	0.02	0.01	0.04	0.01
	M_y	0.01	0.00	-0.07	-0.05	0.00	0.12	0.04	-0.04	-0.01
	M_z	0.03	0.01	0.00	0.02	0.00	-0.01	0.00	-0.01	-0.03
Pylon C	F_x	0.13	-0.26	-0.14	-0.18	-0.06	0.09	-0.14	0.03	0.47
	F_y	0.15	0.02	0.06	0.06	-0.01	0.13	-0.33	-0.16	0.14
	F_z	-0.17	0.04	-0.51	0.09	0.91	0.23	-0.30	-0.27	-0.03
	M_z	-0.02	0.05	0.01	0.02	0.02	-0.10	-0.02	0.03	0.02
	M_y	-0.02	0.02	-0.01	-0.04	-0.02	0.03	0.00	0.06	-0.01
	M_z	0.03	0.02	0.00	0.04	-0.02	-0.03	0.06	-0.02	-0.08
Pylon D	F_x	-0.04	0.28	0.18	-0.31	0.07	0.00	-0.24	-0.07	0.09
	F_y	-0.20	-0.04	-0.11	0.34	-0.05	-0.15	-0.05	0.19	0.10
	F_z	-0.35	0.09	-0.27	-0.01	0.70	0.51	-0.01	-0.32	-0.35
	M_z	-0.03	-0.02	0.01	0.01	-0.03	-0.03	0.00	0.03	0.05
	M_y	-0.13	0.02	0.07	0.07	-0.02	-0.05	0.03	0.07	-0.06
	M_z	0.03	0.01	0.02	0.02	-0.01	-0.02	0.01	-0.02	-0.05

Table 5: Second Prototype Pylon Calibration Error (N) for Points 10-18 (X-Axis Shear and Vertical Loading).

	Load	Point 10	Point 11	Point 12	Point 13	Point 14	Point 15	Point 16	Point 17	Point 18
Pylon A	F_x	-0.39	0.49	-0.92	0.66	-0.44	-0.18	-0.08	0.05	0.81
	F_y	-0.45	-0.04	-0.22	0.52	-0.28	0.18	0.19	0.12	-0.02
	F_z	-0.21	0.41	0.11	0.26	0.14	-0.33	-0.24	-0.10	-0.05
	M_z	-0.07	0.10	-0.02	0.01	0.17	-0.04	-0.03	-0.12	-0.01
	M_y	0.01	0.02	0.00	0.00	-0.05	0.06	-0.01	0.03	-0.06
	M_z	0.08	-0.10	0.07	-0.07	0.06	0.06	-0.01	-0.02	-0.08
Pylon B	F_x	0.35	-0.83	0.17	0.39	-0.12	0.42	-0.25	-0.13	0.03
	F_y	0.11	0.31	-0.18	-0.29	0.30	-0.03	-0.06	-0.68	0.51
	F_z	-0.23	0.40	-0.51	-0.06	0.88	-0.31	-0.02	-0.13	-0.05
	M_z	0.04	0.01	-0.01	-0.07	0.02	0.02	0.02	0.00	-0.03
	M_y	-0.06	0.16	0.03	-0.16	0.04	-0.04	0.06	0.08	-0.11
	M_z	-0.05	0.00	0.02	0.08	-0.08	0.00	-0.03	0.09	-0.04
Pylon C	F_x	0.95	-0.10	0.05	-0.55	-0.31	0.46	-0.33	-0.50	0.36
	F_y	-0.79	-0.38	0.70	1.17	0.17	-1.77	0.06	-0.07	0.90
	F_z	-0.53	0.19	0.34	0.42	0.56	-0.36	-0.58	-0.13	0.10
	M_z	-0.02	0.03	0.06	0.01	-0.05	-0.05	0.03	-0.04	0.04
	M_y	-0.09	0.09	0.07	0.10	-0.07	-0.01	-0.01	-0.10	0.02
	M_z	0.09	0.04	-0.16	-0.17	-0.13	0.22	0.14	0.11	-0.13
Pylon D	F_x	0.04	-0.55	-0.34	0.18	0.18	0.01	0.37	-0.33	0.47
	F_y	0.07	1.05	-0.18	-0.88	-0.68	0.55	0.55	-0.27	-0.21
	F_z	-0.34	0.18	0.09	0.13	0.90	-0.20	-0.57	-0.24	0.06
	M_z	0.04	0.04	-0.01	-0.04	-0.05	0.01	0.03	-0.02	0.00
	M_y	-0.01	0.10	0.00	-0.07	0.12	-0.03	-0.08	-0.02	-0.02
	M_z	-0.08	-0.08	0.13	0.15	0.02	-0.08	-0.13	0.10	-0.03

Table 6: Second Prototype Pylon Calibration Error (N) for Points 19-27 (Y-Axis Shear and Vertical Loading).

	Load	Point 19	Point 20	Point 21	Point 22	Point 23	Point 24	Point 25	Point 26	Point 27
Pylon A	F_x	-0.16	0.09	0.33	0.20	-0.12	0.04	-0.26	-0.14	-0.02
	F_y	0.16	0.08	0.01	-0.04	-0.01	-0.09	-0.18	-0.01	0.07
	F_z	0.03	-0.21	-0.08	0.35	0.15	0.12	-0.14	-0.05	-0.17
	M_z	0.04	0.02	-0.02	-0.06	0.03	-0.06	0.02	0.04	0.00
	M_y	-0.07	0.05	-0.02	-0.01	0.08	0.00	0.01	-0.03	-0.01
	M_z	0.00	-0.02	-0.07	0.04	0.03	0.04	-0.01	0.00	0.00
Pylon B	F_x	0.17	0.41	-0.11	0.13	-1.26	0.25	0.41	0.21	-0.19
	F_y	-0.24	-0.25	-0.03	0.38	0.20	-0.04	0.19	-0.28	0.06
	F_z	-0.14	0.05	-0.04	-0.25	1.10	-0.08	-0.37	0.09	-0.36
	M_z	0.07	-0.04	-0.01	-0.04	0.00	0.01	0.05	-0.03	-0.01
	M_y	0.01	0.03	-0.08	0.01	0.05	0.00	-0.04	0.04	-0.02
	M_z	-0.01	-0.04	-0.02	-0.05	0.18	-0.01	-0.03	-0.06	0.04
Pylon C	F_x	-0.71	0.11	-0.65	0.37	0.80	0.63	0.61	0.00	-1.14
	F_y	0.42	-0.41	0.13	0.55	-0.38	0.32	-0.40	-0.58	0.30
	F_z	-0.22	-0.07	-0.51	0.17	0.93	-0.03	-0.16	0.39	-0.49
	M_z	0.01	-0.04	0.01	0.00	0.03	-0.01	0.01	-0.01	0.02
	M_y	0.09	-0.05	-0.08	0.03	-0.01	0.00	0.02	-0.04	0.04
	M_z	0.05	-0.07	0.12	-0.05	-0.15	0.05	-0.04	-0.05	0.15
Pylon D	F_x	-0.12	0.09	0.10	0.30	1.06	-0.72	0.48	-2.03	0.83
	F_y	-0.49	-0.05	-0.23	0.42	1.07	-0.24	-0.37	0.01	-0.15
	F_z	-0.45	-0.40	-0.37	0.36	0.86	0.44	0.32	0.02	-0.78
	M_z	0.02	0.01	0.01	0.03	-0.01	-0.03	0.01	-0.07	0.05
	M_y	-0.03	-0.01	-0.04	0.08	-0.02	0.00	0.02	-0.03	0.02
	M_z	0.01	-0.02	-0.03	-0.03	-0.18	0.14	-0.06	0.31	-0.14

Once each pylon calibration matrix was tested, test points were then taken on one pylon from each set of prototypes to verify that the prototype designs sufficiently isolated the gaged section of the pylon from the boundary conditions of the pylon. The screws used to mount the pylon to the aluminum mounting plated during calibration were removed from the pylon. The pylon was then rotated 45 degrees about its z-axis, and again screwed down to the aluminum calibration plate. The previously calculated

calibration matrix was left unaltered, and three test data points were taken again by applying the known loads to the calibration device. Point 1 is a 230.4 N vertical load at the center of the pylon, and points 2 and 3 are a 230.4 N vertical load combined with a 91.3 N load 45 degrees between the -X and +Y axes, and 45 degrees between the -X and -Y axes, respectively. Table 7shows the tests points taken, along with the error associated with each test point.

Table 7: Test Point Error for Prototype Pylons after a Change in Mounting.

		F_x	F_y	F_z	F_x Error	F_y Error	F_z Error
Pylon Prototype 1	Point 1	-0.87	0.00	231.81	0.87	0.00	1.41
	Point 2	-64.87	66.00	231.79	0.32	1.45	1.39
	Point 3	-64.74	-66.00	230.61	0.19	1.45	0.21
Pylon Prototype 2	Point 1	-0.65	0.00	231.99	0.65	0.00	1.59
	Point 2	-64.72	-66.00	230.20	0.17	1.45	0.20
	Point 3	-65.65	66.00	231.82	1.10	1.45	1.42

Because the resulting errors were less than the desired 2 N, the pylon calibrations were successfully verified to hold after remounting on a new surface. Although this calibration test confirmed that both sets of prototype pylons were able to maintain calibration with only the one mounting surface constrained, the next step in the testing process required that all four prototype pylons for each set be mounting into a force platform assembly with both pylon mounting surfaces fixed in place.

The final test for the pylons required that a complete force platform, in this case a treadmill assembly, have the calibrated prototype pylons installed. The full treadmill assembly was then calibrated with deadweights to determine if the individual pylon calibrations were valid after the pylons were transferred from the calibration mounting

surface to the force platform mounting surface. To calibrate the complete treadmill assembly, the treadmill top plate of the force platform must be placed upside down. Next, each calibrated pylon was screwed down, and the pylons aligned with pins to ensure that each individual pylon coordinate system is aligned with the global coordinate system of the treadmill, as shown in Figure 48.

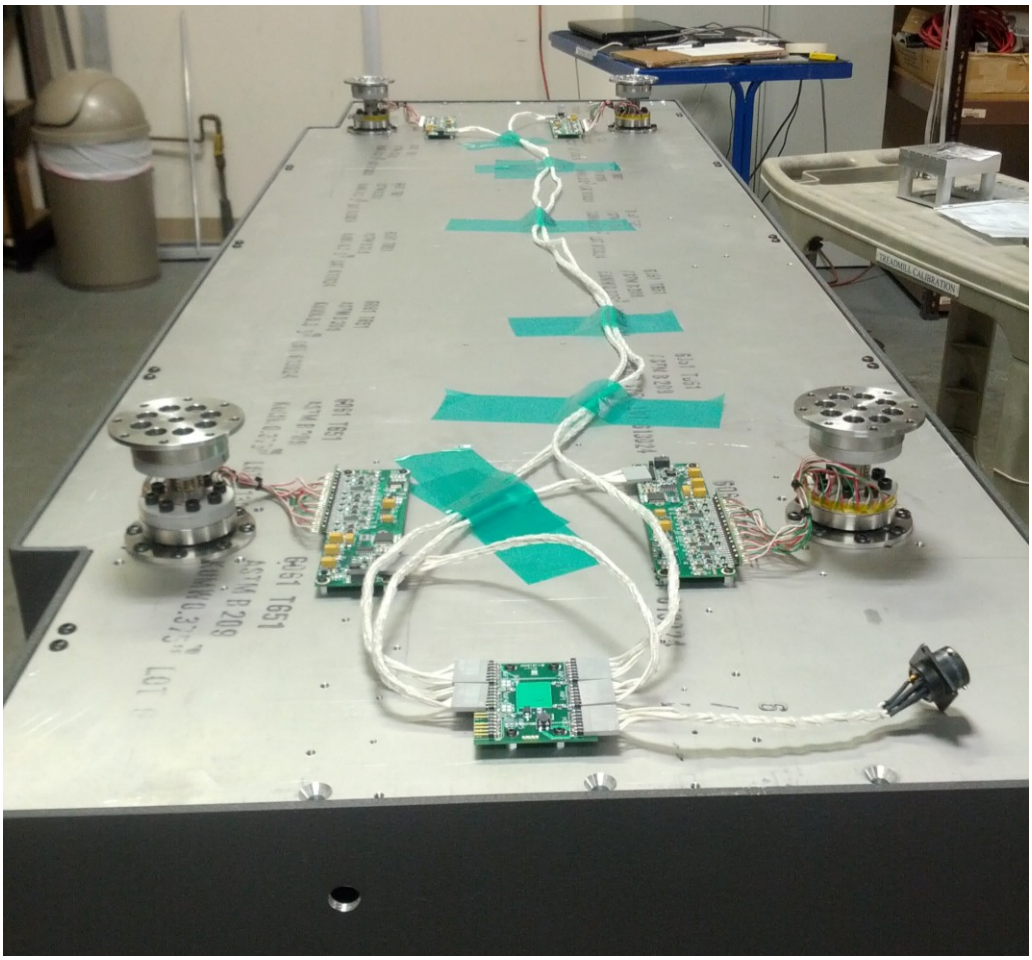

Figure 48: Prototype Pylons Mounted to the Bottom of the Treadmill Force Platform.

Because the bottom pylon mounting flange is inaccessible to tools such as hex keys once the treadmill has been placed on the mounting plate, previous 3-component pylon designs used a nut to clamp the pylon flange to the mounting plate once the treadmill was in position, as shown in Figure 49. For the prototype pylon, however, a simple aluminum plate with threaded holes was first mounted to the bottom flange of the pylon, as shown in Figure 50.

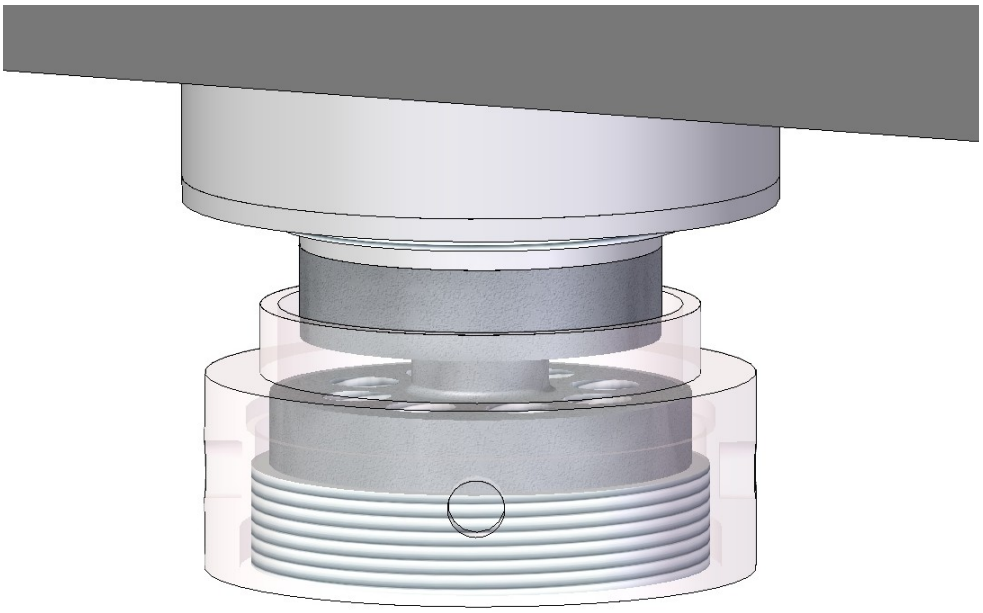

Figure 49: Pylon Nut Mounting Assembly.

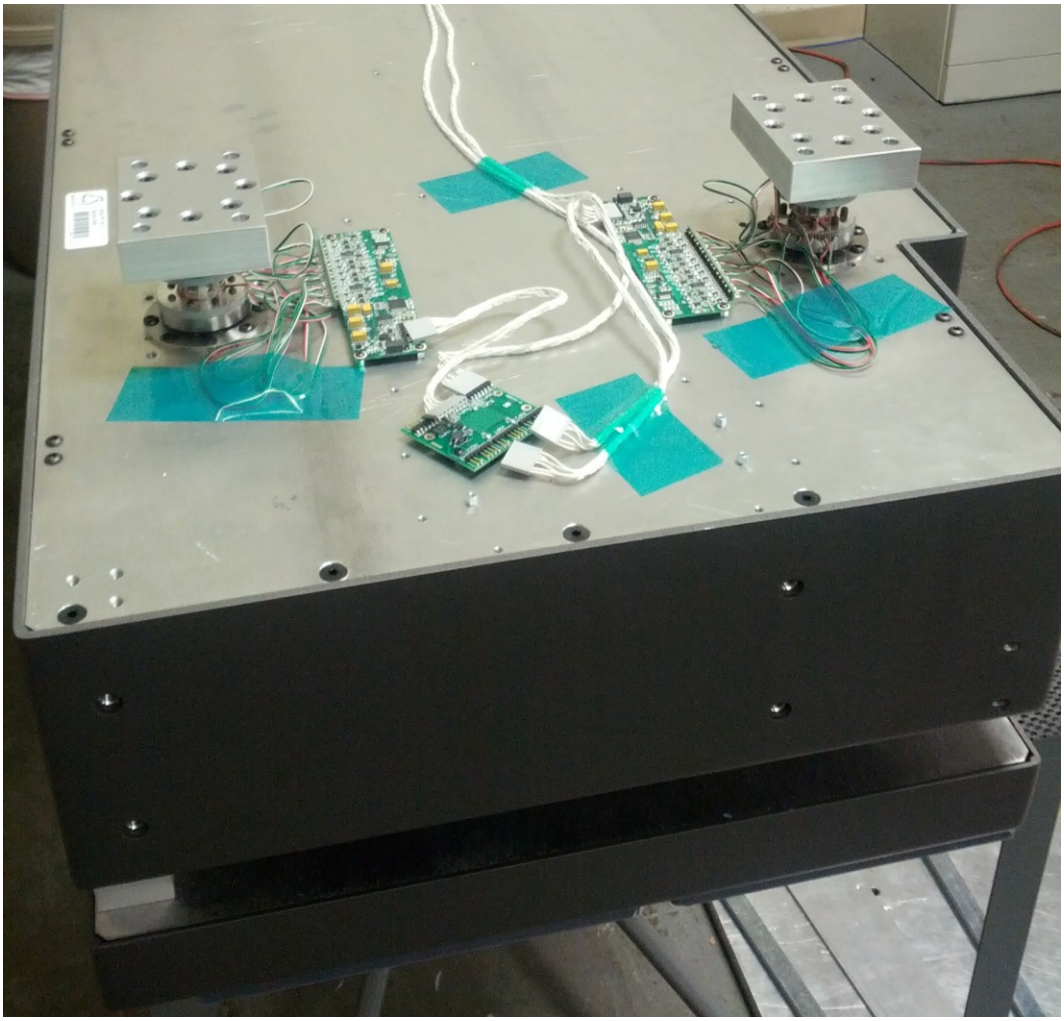

Figure 50: Prototype Pylons Mounted with Aluminum Mounting Blocks.

Next, the force platform assembly was turned over and placed on the mounting plate as shown in Figure 51, and each pylon was zeroed before attaching each of the pylons to the plate with mounting screws.

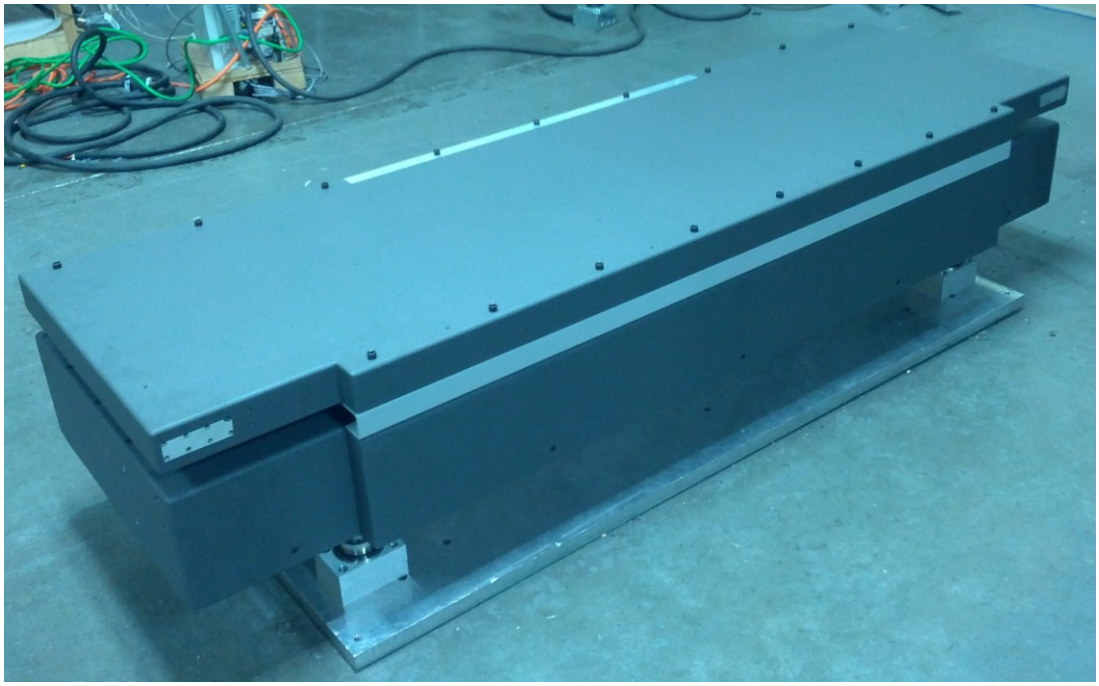

Figure 51: Fully Assembled Treadmill Force Platform with Pylons Mounted.

Finally, 27 test points were taken on the force platform with deadweights applied to the top surface of the platform at 9 points in combination with shear loads in the x and y axis directions. Figure 53 shows the load application points for each test point. The shear loads were applied using a pulley system as shown in Figure 52.

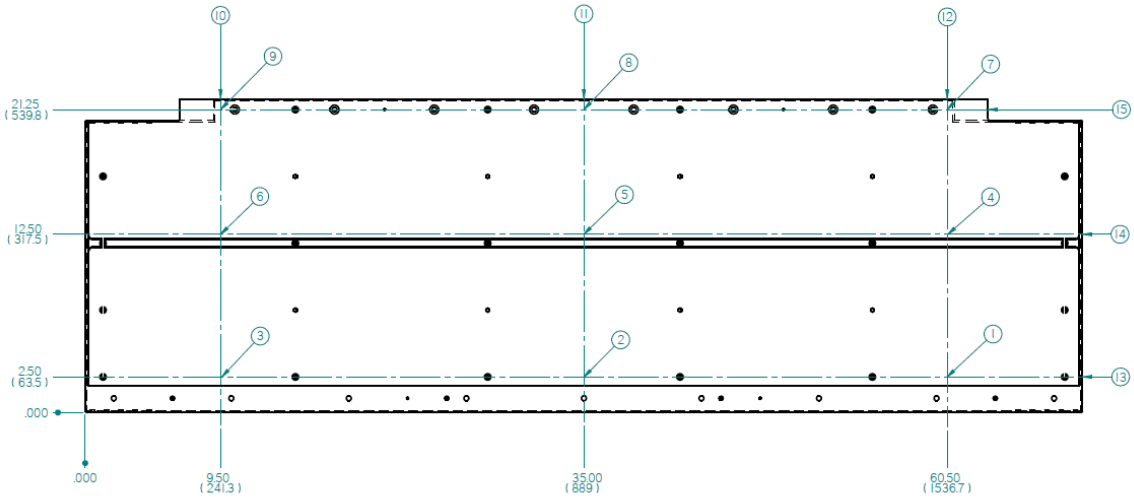

Figure 52: Location of Test Points Taken for Assembled Treadmill Platform.

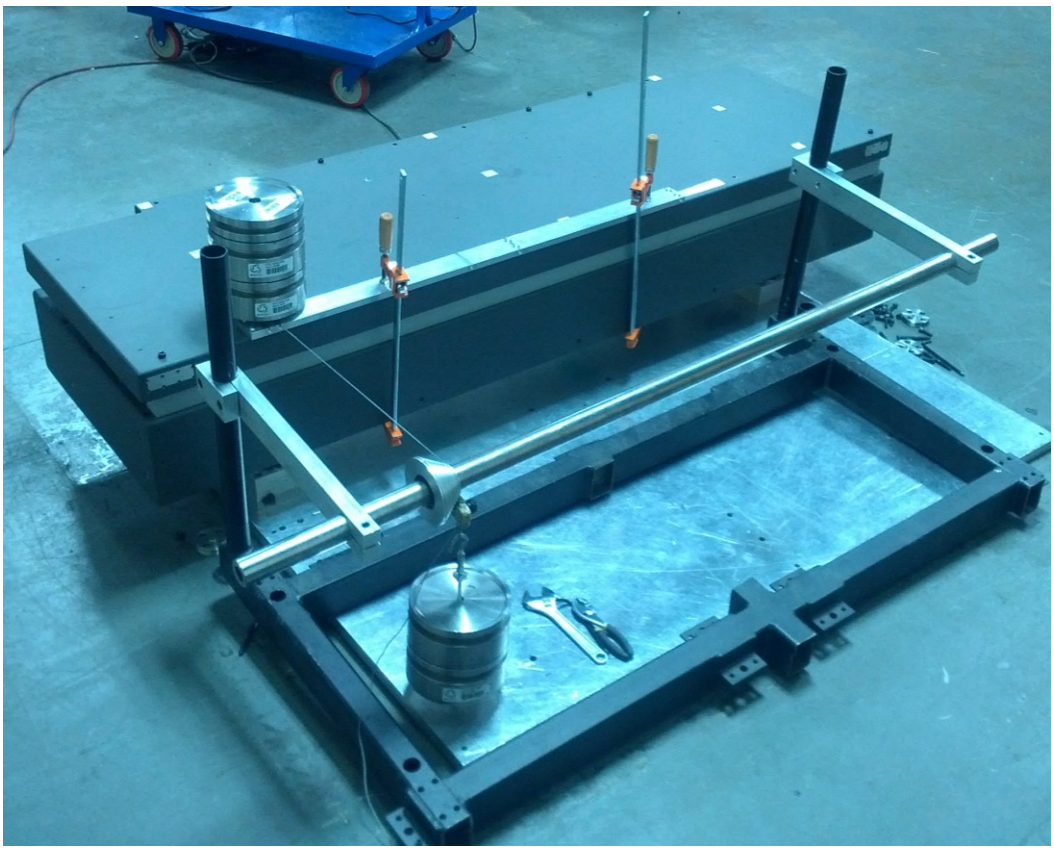

Figure 53: Pulley System Used for Application of Shear and Vertical Loads to Treadmill Assembly.

The test point results showing the measured loads for the first set of prototype pylons are shown in Table 8, while the calculated error of these measured loads from the known deadweights are shown in Table 9.

Table 8: Measured Test Loads for the Treadmill Assembly the First Set of Prototype Pylons.

	F_x (N)	F_y (N)	F_z (N)	M_x (Nm)	M_y (Nm)	M_z (Nm)	CoP_x (m)	CoP_y (m)
Point 1	0.83	-1.55	231.26	54.31	-14.04	-0.08	0.06	0.23
Point 2	0.66	-0.80	231.27	55.62	-73.78	-0.30	0.32	0.24
Point 3	0.02	-0.01	231.50	55.52	-124.86	-0.01	0.54	0.24
Point 4	0.17	-0.13	230.30	203.15	-14.14	0.16	0.06	0.88
Point 5	0.02	-0.08	230.84	204.24	-73.25	-0.01	0.32	0.88
Point 6	-0.99	0.00	231.14	205.47	-124.08	0.05	0.54	0.89
Point 7	0.02	-0.01	228.99	352.45	-14.06	0.02	0.06	1.54
Point 8	-0.40	-0.01	230.68	353.28	-72.99	-0.03	0.32	1.53
Point 9	-1.54	0.00	231.01	354.73	-124.42	0.01	0.54	1.54
Point 10	-184.31	-0.84	231.41	57.20	-15.92	45.75	0.07	0.24
Point 11	-182.73	-0.71	231.83	57.36	-73.99	45.26	0.31	0.24
Point 12	-182.94	-0.56	232.03	57.47	-127.76	45.56	0.54	0.24
Point 13	-181.99	-0.63	231.02	207.62	-14.02	136.04	0.06	0.89
Point 14	-181.35	-0.19	231.55	206.13	-74.00	160.43	0.32	0.89
Point 15	-182.21	0.00	231.81	206.39	-125.33	160.56	0.54	0.89
Point 16	-181.55	-1.94	231.20	355.10	-14.54	276.90	0.06	1.54
Point 17	-182.30	0.78	231.61	355.99	-74.22	279.60	0.32	1.54
Point 18	-181.73	1.70	232.37	357.82	-124.58	278.88	0.54	1.54
Point 19	1.96	-184.73	231.10	56.16	-15.77	-11.98	0.07	0.24
Point 20	2.00	-184.63	231.05	206.06	-15.83	-12.19	0.07	0.89
Point 21	1.99	-184.70	231.07	354.72	-15.81	-10.84	0.07	1.54
Point 22	-1.94	-184.95	232.14	57.22	-73.06	-58.00	0.31	0.25
Point 23	-1.97	-184.90	231.58	206.14	-73.13	-58.00	0.32	0.89
Point 24	-0.63	-184.52	232.49	356.15	-73.26	-58.00	0.32	1.53
Point 25	-1.83	-184.26	232.05	56.85	-125.00	-100.32	0.54	0.25
Point 26	-1.83	-184.75	230.14	205.50	-125.00	-101.92	0.54	0.89
Point 27	-1.80	-184.28	230.13	354.81	-125.00	-101.90	0.54	1.54

Table 9: Calculated Errors of the Treadmill Assembly with the First Set of Prototype Pylons.

	F_x (N)	F_y (N)	F_z (N)	CoP_x (m)	CoP_y (m)
Point 1	0.83	1.55	0.86	0.003	0.006
Point 2	0.66	0.80	0.87	0.002	0.001
Point 3	0.02	0.01	1.10	0.000	0.001
Point 4	0.17	0.13	0.10	0.002	0.007
Point 5	0.02	0.08	0.44	0.000	0.004
Point 6	0.99	0.00	0.74	0.003	0.000
Point 7	0.02	0.01	1.41	0.002	0.002
Point 8	0.40	0.01	0.28	0.001	0.005
Point 9	1.54	0.00	0.61	0.001	0.001
Point 10	1.71	0.84	1.01	0.004	0.003
Point 11	0.13	0.71	1.43	0.004	0.002
Point 12	0.34	0.56	1.63	0.001	0.002
Point 13	0.61	0.63	0.62	0.004	0.002
Point 14	1.25	0.19	1.15	0.002	0.001
Point 15	0.39	0.00	1.41	0.001	0.001
Point 16	1.05	1.94	0.80	0.001	0.001
Point 17	0.30	0.78	1.21	0.003	0.000
Point 18	0.87	1.70	1.97	0.004	0.003
Point 19	1.96	2.13	0.70	0.005	0.002
Point 20	2.00	2.03	0.65	0.005	0.003
Point 21	1.99	2.10	0.67	0.005	0.002
Point 22	1.94	2.35	1.74	0.003	0.005
Point 23	1.97	2.30	1.18	0.002	0.001
Point 24	0.63	1.92	2.09	0.002	0.005
Point 25	1.83	1.66	1.65	0.001	0.004
Point 26	1.83	2.15	0.26	0.003	0.004
Point 27	1.80	1.68	0.27	0.003	0.005

Based on these calibration results, it can be concluded that the first set of independently calibrated 6-component prototype pylons were able to be transferred to the force platform mounting surfaces and accurately measure GRF's on the top surface of the platform to within 2 N, as well as maintain CoP accuracy within 10 mm across most of the platform. Although errors are still present in the GRF measurement and CoP

calculation, the maximum errors are no greater than previous 3-component load cell treadmill designs.

Although the second set of prototype pylons performed similarly to the first set of prototype pylons during calibration, there was a noticeable performance difference when mounted in the force platform assembly. When pure vertical loads were applied to the top surface of the force platform, the load cells were erroneously measuring additional shear loads of up to 30 N. To determine if the erroneous shear loads were being caused by the surface mounting conditions of the pylons, the pylons were first dismounted from the mounting plate by removing the fasteners from each pylon mounting block. With the fasteners removed, each pylon was able to rest on the ground and slide in place unconstrained. However, the erroneous shear loads of up to 30 N continued to be measured with this setup. As a final effort to identify the issue causing the erroneous, a single ball bearing was placed on the bottom of each pylon, while the entire force platform assembly rested on the mounting plate. The ball bearing setup, shown in Figure 54, ensured that the pylons would contact the mounting plate at a single point, reducing the effect of surface mounting conditions on the pylons. In fact, while the treadmill pylons rested on the ball bearings, the shear errors seen while applying a pure vertical load were reduced from 30 N to less than 2 N.

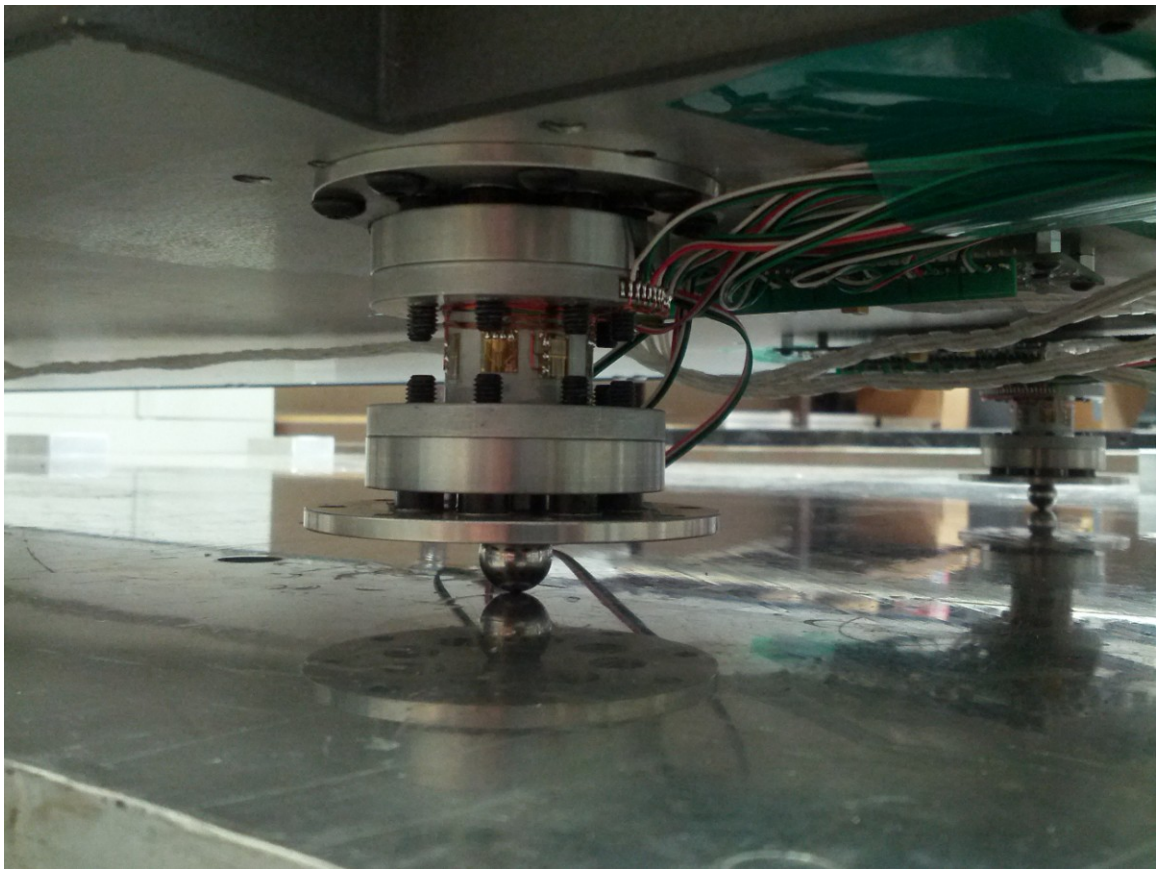

Figure 54: Ball Bearing Setup Used to Test the Second Set of Prototype Pylons.

Although not a practical setup for actual operation of the treadmill, the ball bearing setup did confirm that it was the pylon surface mounting conditions that were causing the erroneous shear loads. Additionally, the physical testing confirmed the second pylon's underperformance in the FEM simulation for the non-parallel surface loading conditions.

With the calibration data for the first and second prototype designs collected, the testing process was then continued for only the first prototype design. The treadmill assembly with the first prototype pylon set was tested to verify that the natural frequency

of the treadmill system was maintained or increased from the previous pylon design. In order to empirically determine the natural frequency of the system, a treadmill was assembled first with a set of the previous pylons, and then with a set of the successful prototype pylons. Next, the treadmill was instrumented with an accelerometer, as shown in Figure 55, and the top surface was hit with a nylon tipped mallet to excite free vibrations in the system.

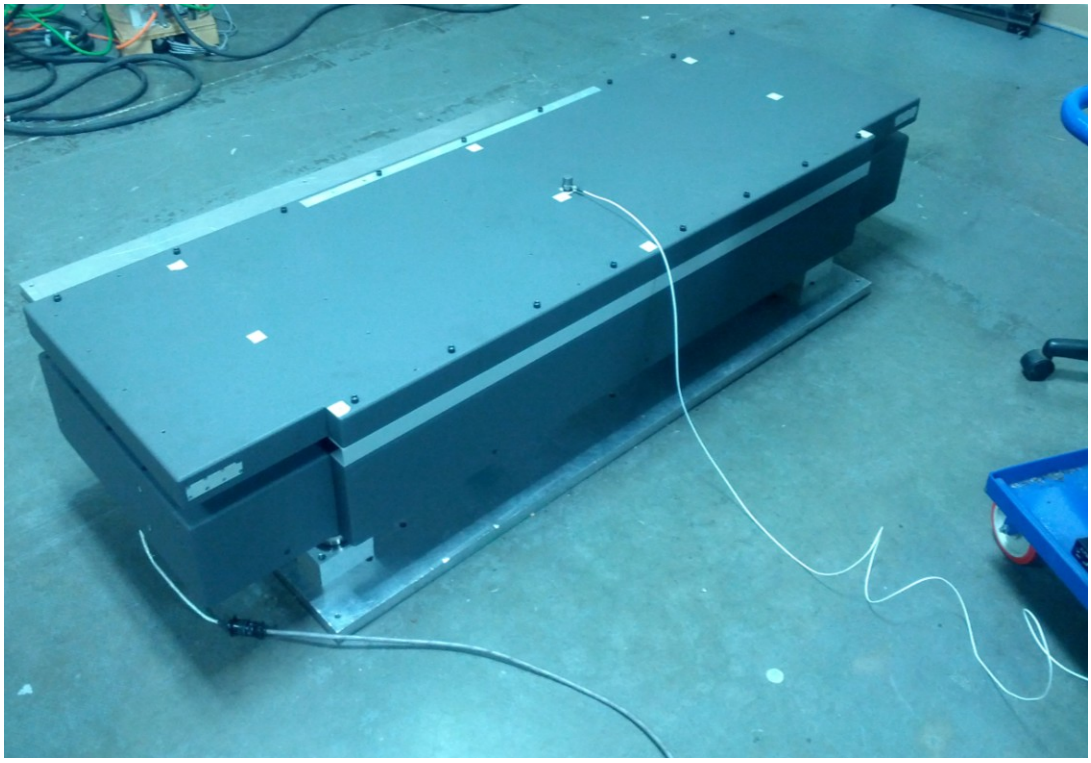

Figure 55: Accelerometer Placement on the Treadmill Force Platform.

The raw data from the accelerometer was then converted to a fast Fourier transform (FFT) plot using MATLAB. The resulting FFT plot for the treadmill with the current pylon design and the first prototype design are shown in Figure 56. The position

of the major peaks in the FFT plot at 44Hz for the current design and 53Hz for the prototype design confirms that the natural frequency of the system is slightly increased by the new pylon design.

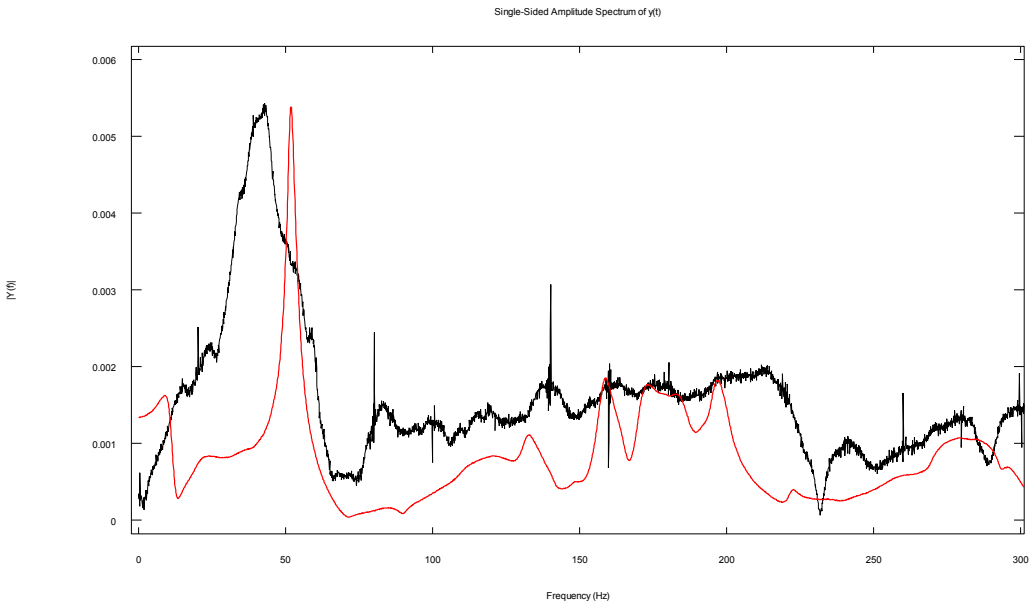

Figure 56: FFT Plot Showing the Original Pylon (Black) and First Prototype Pylon (Red) Accelerometer Results.

Chapter 4: Discussion

The prototype pylon using the stainless steel spacers and standard 0.75" OD, 0.875" tall pylons performed well in the individual calibration, remounting, and resulting treadmill assembly. Having a process for individually calibrating the pylons and removing for later assembly allows for a drastic change in the calibration process. Instead of requiring 8 hours for a full treadmill calibration, the calibration process with 6-component pylons may be developed into a semi-automated process. With the boundary conditions of the prototype pylons sufficiently isolated from the mounting conditions, the pylons may now be calibrated on one surface, such as an automated rotary table or x-y table, and moved to the treadmill assembly after calibration. The concept of calibration on a mobile mounting surface would allow for load application by automated means such as a pneumatic or electric actuators, potentially reducing the calibration time of an entire treadmill to minutes rather than hours.

It is possible that the errors present in the force and CoP measurement are a direct result of the calibration process itself. Although applying load components in the vertical direction and in midline of the pylon for shear reduced errors due to the moments on the pylon, there are still potential errors in the this calibration method simply because the unconstrained mounting of the individual pylon does not precisely duplicate the loading that the pylon will experience in the installed treadmill platform. An alternative

calibration method could be done after the treadmill is installed, using a wand-like tool to apply loads in known quantities at known angles to the top surface of the treadmill. Unfortunately this alternative calibration method would require accurate positioning and orientation of the wand, as well as a controlled and known value for the load magnitude. It is also worth noting that these calibrations were done with the assumption that a linear fit of the calibration matrices is valid across the entire treadmill surface. However, because force plate errors tend to increase towards the edges of the plate, it is possible that a nonlinear calibration model would provide a better overall calibration. However, without improvements to the amplifier electronics to reduce measurement drift and improve strain gage zeroing, a nonlinear calibration is currently unfeasible.

References

Belli, Alain, Phong Bui, Antoine Berger, Andre Geyssant, Jean-Rene Lacour (2001). A treadmill ergometer for three-dimensional ground reaction forces measurement during walking. Journal of Biomechanics, Volume 34, Page 105–112.

Berme, Necip (2001). U.S. Patent No. 6,295,878 B1. Washington, DC: U.S. Patent and Trademark Office.

Berme, Necip (2002). U.S. Patent No. 6,354,155 B1. Washington, DC: U.S. Patent and Trademark Office.

Bisseling, Rob W., A. L. Hof (2006). Handling of impact forces in inverse dynamics. Journal of Biomechanics, Volume 39, Page 2438–2444.

Brand, R. A., R. D. Crowninshield, R. C. Johnston, and J. G. Andrews (1978). A biomechanical investigation of the human hip. Journal of Biomechanics, Volume 11, Page 75–85.

Brown, G.W., and D.M Cunningham (1952). Two Devices for Measuring The Forces Acting on the Human Body During Walking. Proceedings of the Society for Experimental Stress Analysis, Volume IX, Number 2, Page 75.

Carignan, F.J. et al (1985). U.S. Patent No. 4,493,220. Washington, DC: U.S. Patent and Trademark Office.

Chockalingam, Nachiappan, Giannis Giakas, Anna Iossifidou (2002). Do strain gauge force platforms need in situ correction?. Gait and Posture, Volume 16, Page 233–237.

Desjardins, P., A. Plamondon, M. Gagnon (1998). Sensitivity analysis of segment models to estimate the net reaction moments at the L5/S1 joint in lifting. Mechanical Engineering and Physics, Volume 20, Page 153–158.

Dierick, Frédéric, Massimo Penta , David Renaut, Christine Detrembleur (2004). A force measuring treadmill in clinical gait analysis. Gait and Posture, Volume 20, Page 299–303.

Heglund, Norman C. (1981). A simple design for a force -plate to measure ground reaction forces. Journal of Experimental Biology, Volume 93, Page 333–338.

Kram, Rodger, Timothy M. Griffin, J. Maxwell Donelan, and Young Hui Chang (1998). Force treadmill for measuring vertical and horizontal ground reaction forces. Journal of applied physiology, Volume 85, Number 2, Page 764–769.

Lord, Marilyn (1981). Foot Pressure Measurement: A Review of Methodology. Journal of Biomedical Engineering, Volume 3, Page 91–99.

Miyazaki, S. and H. Iwakura (1978). Foot-Force Measuring Device for Clinical Assessment of pathological gait. Medical & Biological Engineering & Computing, Volume 16, Page 429–436.

Riemer, Raziel, Elizabeth T. Hsiao-Wecksler, Xudong Zhang (2008). Uncertainties in inverse dynamics solutions: A comprehensive analysis and an application to gait. Gait and Posture, Volume 27, Page 578–588.

Appendix: Calibration Matrix Code

MATLAB code used to calculate the calibration matrix for each 6-component pylon, along with the associated error matrix.

```
% This program calibrates a 6 component pylon (27 point cal from one file)
clear
N = 27;   % number of calibration points
ch = 8;  % number of channels

load Calibration2.txt;
A=Calibration2;
%s = transpose(A);
%********** Calibration Points & Loads **********
Lv = 230.3;   % vertical load
Lx = 182.6;   % x-shear load
Ly = 182.6;   % y-shear load
dy = .01905;
dx = .01905;
z1 = .0352;
fori = 1:9,
f(i,:) = [0 0 Lv];
end
fori = 10:18,
f(i,:) = [-Lx 0 Lv];
end
fori = 19:27,
f(i,:) = [0 Ly Lv];
end
```

```
p(1,:) = [dx -dy -z1];
p(2,:) = [dx -0 -z1];
p(3,:) = [dx dy -z1];
p(4,:) = [0 -dy -z1];
p(5,:) = [0 0 -z1];
p(6,:) = [0 dy -z1];
p(7,:) = [-dx -dy -z1];
p(8,:) = [-dx 0 -z1];
p(9,:) = [-dx dy -z1];
p(10,:) = [dx -dy -z1];
p(11,:) = [dx -0 -z1];
p(12,:) = [dx dy -z1];
p(13,:) = [0 -dy -z1];
p(14,:) = [0 0 -z1];
p(15,:) = [0 dy -z1];
p(16,:) = [-dx -dy -z1];
p(17,:) = [-dx 0 -z1];
p(18,:) = [-dx dy -z1];
p(19,:) = [dx -dy -z1];
p(20,:) = [dx -0 -z1];
p(21,:) = [dx dy -z1];
p(22,:) = [0 -dy -z1];
p(23,:) = [0 0 -z1];
p(24,:) = [0 dy -z1];
p(25,:) = [-dx -dy -z1];
p(26,:) = [-dx 0 -z1];
p(27,:) = [-dx dy -z1];
%********************* Load Vector *********************************
fori = 1:N,
L(i,1:3) = f(i,:);
L(i,4:6) = cross(p(i,:),f(i,:));
end
%********************* Compute Matrix *********************************
C = (pinv(A')*L)';
e = C*A-L';
fid = fopen('C_PylonA.txt','wt');
fprintf(fid,'%15.5e %15.5e %15.5e %15.5e %15.5e %15.5e %15.5e %15.5e\n',(C(1,:))');
fprintf(fid,'%15.5e %15.5e %15.5e %15.5e %15.5e %15.5e %15.5e %15.5e\n',(C(2,:))');
fprintf(fid,'%15.5e %15.5e %15.5e %15.5e %15.5e %15.5e %15.5e %15.5e\n',(C(3,:))');
fprintf(fid,'%15.5e %15.5e %15.5e %15.5e %15.5e %15.5e %15.5e %15.5e\n',(C(4,:))');
fprintf(fid,'%15.5e %15.5e %15.5e %15.5e %15.5e %15.5e %15.5e %15.5e\n',(C(5,:))');
fprintf(fid,'%15.5e %15.5e %15.5e %15.5e %15.5e %15.5e %15.5e %15.5e\n',(C(6,:))');
save Errors.txt e;
fclose(fid);
```